

This is an Open Access document downloaded from ORCA, Cardiff University's institutional repository: <https://orca.cardiff.ac.uk/id/eprint/159422/>

This is the author's version of a work that was submitted to / accepted for publication.

Citation for final published version:

Martin, Andrew J., McDonald, Iain, Jamieson, John W., Jenkin, Gawen R. T., McFall, Katie A., Piercey, Glenn, MacLeod, Christopher J. and Layne, Graham D. 2021. Mineral-scale variation in the trace metal and sulfur isotope composition of pyrite: implications for metal and sulfur sources in mafic VMS deposits. *Mineralium Deposita* 57 (6) , pp. 911-933. 10.1007/s00126-021-01080-1

Publishers page: <http://dx.doi.org/10.1007/s00126-021-01080-1>

Please note:

Changes made as a result of publishing processes such as copy-editing, formatting and page numbers may not be reflected in this version. For the definitive version of this publication, please refer to the published source. You are advised to consult the publisher's version if you wish to cite this paper.

This version is being made available in accordance with publisher policies. See <http://orca.cf.ac.uk/policies.html> for usage policies. Copyright and moral rights for publications made available in ORCA are retained by the copyright holders.



1 **Mineral-scale variation in the trace metal and sulfur isotope composition of pyrite:**  
2 **Implications for metal and sulfur sources in mafic VMS deposits**

3 Andrew J. Martin<sup>1\*</sup>, Iain McDonald<sup>2</sup>, John W. Jamieson<sup>1</sup>, Gawen R.T. Jenkin<sup>3</sup>, Katie A. McFall<sup>1</sup>, Glenn  
4 Piercey<sup>4</sup>, Christopher J. MacLeod<sup>1</sup> and Graham D. Layne<sup>1</sup>

5 <sup>1</sup>Department of Earth Sciences, Memorial University of Newfoundland, Canada

6 <sup>2</sup>School of Earth and Environmental Sciences, Cardiff University, UK

7 <sup>3</sup>School of Geography, Geology and the Environment, University of Leicester, UK

8 <sup>4</sup>MAF-IIC SIMS Facility, Memorial University of Newfoundland, Canada

9 \* Corresponding author: [ajmartin@mun.ca](mailto:ajmartin@mun.ca)

10 **Abstract**

11 The link between metal enrichment and the addition of a magmatic volatile phase in volcanogenic massive  
12 sulfide deposits and actively forming seafloor massive sulfide deposits remains poorly characterized. This  
13 is especially true when considering how metal, sulfur and fluid flux change with time. In this study we  
14 combine *in situ* sulfur isotope ( $\delta^{34}\text{S}$ ; n=31) measurements with trace metal chemistry of pyrite (n=143) from  
15 the Mala VMS deposit, Troodos, Cyprus. The aim of our study is to assess the links between volatile influx  
16 and metal enrichment and establish how, or indeed if, this is preserved at the scale of individual mineral  
17 grains. We classify pyrite based on texture into colloform, granular, disseminated and massive varieties.  
18 The trace metal content of different pyrite textures is highly variable and relates to fluid temperature and  
19 secondary reworking that are influenced by the location of the sample within the mound. The sulfur isotope  
20 composition of pyrite at Mala ranges from -17.1 to 7.5‰ (n=31), with a range of -10.9 to 2.5‰ within a  
21 single pyrite crystal. This variation is attributed to changes in the relative proportion of sulfur sourced from  
22 i)  $\text{SO}_2$  disproportionation, ii) thermochemical sulfate reduction, iii) the leaching of igneous sulfur/sulfide  
23 and, iv) bacterial sulfate reduction. Our data shows that there is no correlation between  $\delta^{34}\text{S}$  values and the

24 concentration of volatile elements (Te, Se) and Au in pyrite at Mala indicating that remobilization of trace  
25 metals occurred within the mound.

## 26 Introduction

27 The source of metals in volcanogenic massive sulfide (VMS) and actively forming seafloor massive sulfide  
28 (SMS) deposits remains poorly constrained and actively debated (Sillitoe et al. 1996; Yang and Scott 1996;  
29 Jowitt et al. 2012; Keith et al. 2018; Martin et al. 2020; Patten et al. 2020). Principally, two metal sources  
30 can contribute to the metal budget of VMS deposits: leaching of metals from underlying host rocks during  
31 hydrothermal alteration (Richardson et al. 1987; Jowitt et al. 2012; Banerjee et al. 2000; Patten et al. 2017);  
32 and the addition of a magmatic volatile phase to the overlying hydrothermal system (Yang and Scott 1996,  
33 2002; de Ronde et al. 2011; Martin et al. 2020, 2021; Patten et al. 2020). The relative contribution of metals  
34 from these two sources and how they change with system maturity (i.e. time) and the subsequent  
35 preservation of trace metal signatures to distinguish these sources in sulfide minerals in VMS deposits  
36 remains enigmatic. Here, we apply *in situ* geochemical and sulfur isotope measurements on pyrite from the  
37 92 million year old Mala VMS deposit of the Troodos ophiolite (Cyprus) to assess co-variations in trace  
38 metal content and sulfur isotope ratios ( $\delta^{34}\text{S}$ ) in an ancient mafic VMS deposit. These data will be used to  
39 investigate the variability in metal and sulfur sources during the growth of individual pyrite crystals and to  
40 understand if the influx of certain volatile metals can be linked to variations in sulfur isotopic composition.

41 To investigate the source(s) of metals in VMS deposits, previous studies utilized either trace metal  
42 enrichment profiles (Halbach et al. 1998; Butler and Nesbitt 1999; Maslennikov et al. 2009; Wohlgemuth-  
43 Ueberwasser et al. 2015; Keith et al. 2016a; Grant et al. 2018; Wang et al. 2018), the ratio of Se to S  
44 (Yamamoto 1976; Huston et al. 1995; Hannington et al. 1999; Layton-Matthews et al. 2008, 2013; Martin  
45 et al. 2019), or the sulfur isotopic composition of sulfide minerals (Herzig et al. 1998; Gemmell et al. 2004;  
46 Huston et al. 2011; Yeats et al. 2014; Brueckner et al. 2015; Lode et al. 2017; Zeng et al. 2017). However,  
47 very few studies utilize a combined approach (e.g., Rouxel et al. 2004; Sharman et al. 2015; Meng et al.

48 2020; Martin et al. 2021) that takes into consideration any systematic relationship between trace element  
49 enrichment profiles and the sulfur isotopic composition of sulfide minerals; this is especially true when  
50 considering the complex nature of different pyrite textures, generations (i.e. overgrowths) and variation that  
51 occurs at the scale of individual mineral grains.

52 In volatile-rich, subduction influenced VMS deposits, the systematic enrichment of certain metals such as  
53 Pb, As, Sb, Bi, Hg and Te (Wohlgemuth-Ueberwasser et al. 2015), Se, Cu and Te (Keith et al. 2016a), Bi  
54 and Te (Mathieu 2019) or Se, Cu, Te and Au (Martin et al. 2021) have been proposed to indicate the addition  
55 of a metal-rich magmatic volatile phase to the hydrothermal system from degassing of shallow magma  
56 reservoirs (e.g., Huston et al. 2011). Additionally, elevated Se/S (expressed as  $\text{Se/S} \cdot 10^6$ ) that are  $>500$  in  
57 pyrite are also interpreted as representing an increased magmatic volatile influx in VMS deposits  
58 (Yamamoto 1976; Huston et al. 1995; Layton-Matthews et al. 2008, 2013). The sulfur isotopic composition  
59 of sulfide minerals provides further evidence of a magmatic volatile contribution to VMS deposits with the  
60 addition of degassing magmatic  $\text{SO}_2$  that undergoes disproportionation upon mixing with hydrothermal  
61 fluid, and results in a characteristic sulfur isotope composition defined by  $\delta^{34}\text{S}$  values that are less than the  
62 magmatic mean ( $<0\%$ , MORB; Herzig et al. 1998; Kusakabe et al. 2000; de Ronde et al. 2005). These low  
63  $\delta^{34}\text{S}$  values are generally limited to felsic or subduction influenced environments (e.g., Herzig et al. 1998;  
64 Huston et al. 2011), where magmas are more volatile-rich relative to mafic hosted mid-ocean ridge (MOR)  
65 environments (Wallace 2005). However, this signature was also recorded in an ancient mafic VMS deposit  
66 (Martin et al. 2021). This sulfur isotope composition contrasts signatures typical of MOR environments,  
67 where  $\delta^{34}\text{S}$  values in sulfide minerals are positive, indicating a combination of sulfur from thermochemical  
68 sulfate reduction (TSR) of seawater at high temperatures ( $>160^\circ\text{C}$ ) in the presence of iron-bearing minerals  
69 and leaching of sulfur and primary igneous sulfide minerals from igneous host rocks (Ono et al. 2007).

70 Previous studies utilising laser ablation inductively coupled plasma mass spectrometry (LA-ICP-MS) of  
71 sulfide minerals from Troodos VMS deposits indicate that deposits associated with the Solea graben, one  
72 of three fossil spreading axes in the Troodos ophiolite are enriched in Se, Cu and Au (Keith et al. 2016a;

73 Fig. 1). The enrichment of these elements is attributed to the contribution of a magmatic volatile phase to  
74 the hydrothermal systems of the Solea graben (Martin et al. 2019, 2020).

75 Variation in the sulfur isotope composition of pyrite has largely been constrained in Troodos VMS deposits  
76 using whole-rock analytical methods of sulfide minerals with the median composition for all Troodos VMS  
77 sulfide minerals of  $4.6 \pm 2.7\text{‰}$  ( $1\sigma$ ,  $n=220$ ) indicating that sulfur is primarily sourced from both the leaching  
78 of igneous sulfur/sulfide and TSR of seawater (Hannington et al. 1998; Parvaz 2014; Keith et al. 2016a;  
79 Pedersen et al. 2017; Martin et al. 2020). However, significant variation is noted in the sulfur isotope  
80 composition of pyrite across Troodos VMS deposits with the  $\delta^{34}\text{S}$  values of pyrite ranging from  $-7.6\text{‰}$  to  
81  $13.2\text{‰}$  (Martin et al. 2020, 2021). Samples of disseminated pyrite that occur within the volcanic  
82 stratigraphy exhibit significantly lower  $\delta^{34}\text{S}$  values than those typical for Troodos VMS deposits; pyrite is  
83 depleted in  $^{34}\text{S}$ , with  $\delta^{34}\text{S}$  values ranging from  $-22.2\text{‰}$  to  $-6.9\text{‰}$ . These values indicate that bacterial sulfate  
84 reduction (BSR) occurred at low temperatures ( $<120^\circ\text{C}$ ) in the shallow subsurface, away from areas of high  
85 temperature fluid discharge (Pedersen et al. 2017).

86 Sulfide mineral chemistry and the sulfur isotopic composition of sulfide minerals analysed using bulk  
87 analytical techniques leads to the homogenization of any variation in the chemical and isotopic composition  
88 of the sample. Thus, there is a need to apply *in situ* analytical techniques to better understand the spatial  
89 zonation in isotopic and chemical composition within individual mineral grains. Utilizing a combined  
90 approach of *in situ* LA-ICP-MS analysis to measure trace metal concentrations and Secondary Ion Mass  
91 Spectrometry (SIMS) to measure sulfur isotope ratios, this study aims to establish if links exist between  
92 trace metal enrichment and variations in the source of sulfur during VMS deposit formation. We focus on  
93 the Mala VMS deposit located in the Troodos ophiolite of Cyprus, as Mala represents an immature  
94 magmatic volatile-influenced deposit where links between magmatic volatile influx, sulfur isotope ratios  
95 and trace metal enrichment signatures in pyrite have not been extensively modified during fluid  
96 overprinting associated with the maturation of the VMS mound (Martin et al. 2021). We present *in situ*  
97 sulfur isotope data and trace element geochemistry of different pyrite textures that highlight variable trace

98 element enrichment profiles that can be related to mound-scale fluid flow. We then combine trace metal  
99 geochemistry and sulfur isotope ratios to test if any systematic relationship exists between magmatic  
100 volatile influx and the enrichment of Te, Se and Au in pyrite at Mala.

## 101 Geological Setting

102 The 92 Ma Troodos ophiolite in Cyprus comprises a complete, un-deformed oceanic pseudo-stratigraphy  
103 (Gass 1968; Mukasa and Ludden 1987). Mantle peridotites are surrounded radially by gabbro and  
104 plagiogranite of the plutonic sequence, a sheeted dyke complex (SDC), and the basal group (BG), which  
105 consists of a transitional horizon between the SDC and overlying upper and lower pillow lavas (UPL-LPL;  
106 Fig. 1) (Gass 1968). It has long been recognized that the Troodos ophiolite formed in a sediment-free  
107 subduction influenced environment due to the occurrence of boninite (Pearce and Robinson 2010; Woelki  
108 et al. 2018), the trace element and isotopic composition of volcanic glass (Rautenschlein et al. 1985),  
109 elevated H<sub>2</sub>O contents of parent melts (>2 wt.% H<sub>2</sub>O; Muenow et al. 1990), and an enrichment of magmatic  
110 volatile derived elements (e.g., Te, Se) in some VMS deposits (Keith et al. 2016b; Martin et al. 2019, 2021).

111 Observations from actively forming intermediate to slow seafloor spreading centers are akin to processes  
112 and structures preserved in the Troodos ophiolite (Varga and Moores 1985). On the northern flank of the  
113 ophiolite, three structural grabens are delineated by inversely dipping sheeted dykes along a series of  
114 ~north-south normal faults (Varga and Moores 1985). The grabens from east to west are; Larnaca, Mitsero  
115 and Solea (Fig. 1). The grabens are widely accepted as representing fossil axial spreading ridges (Varga  
116 and Moores 1985). Associated with these graben bounding faults are VMS deposits that formed within or  
117 at the contact between the BG, LPL and UPL units at the periphery of the ophiolite that once represented  
118 the Cretaceous seafloor (Hannington et al. 1998; Adamides 2010; Fig. 1).

119 Hydrothermal alteration of the Troodos crust is well-characterized and the leaching of metals from the SDC  
120 during spilitisation and epidosite formation is interpreted as a possible source of metal and sulfur in  
121 overlying VMS deposits (Richardson et al. 1987; Jowitt et al. 2012; Patten et al. 2017). More recently, a

122 pulsed magmatic volatile component has been suggested as an additional source of some metals (Cu, Au,  
123 Te and Se) in Troodos VMS deposits, especially in magmatic volatile-influenced VMS deposits such as  
124 Mala and deposits associated with the Solea graben in particular (Keith et al. 2016a; Martin et al. 2020; Fox  
125 et al. 2020).

## 126 The Mala VMS deposit

127 The Mala VMS deposit is located in the southwest Troodos ophiolite, northwest of the town of Pano Pangia  
128 within the Pafos Forest region (Fig. 1). Mala is located deep in the lava stratigraphy at the BG-LPL  
129 transition. Previous studies have identified an enrichment in Te, Se, Cu and Au in pyrite at Mala relative to  
130 other Troodos VMS deposits (Martin et al. 2021). Mala has been historically mined for Cu and Zn (0.8 Mt  
131 total; Brazilian Metals Group, 2013) leading to the exposure of a massive sulfide mound at the northern  
132 end of the open pit (Fig. 2).

133 The exposed pyrite mound measures approximately 12 x 8 m (width x height) and contains pyrite and  
134 gypsum (Fig. 2A). Gypsum occurs as three distinct morphologies: massive-bedded, breccia infill, and mesh  
135 textured varieties (Fig. 2B-G). Within the gypsum are euhedral pyrite crystals which vary in size from <1  
136 mm up to 2 cm in width (Fig. 2D-G). In the VMS mound pyrite forms as five distinct textures: massive  
137 euhedral grains (Fig. 3A), dendritic growths (Fig. 3B and C), colloform bands (Fig. 3D), granular pyrite  
138 (Fig 3E) and as disseminated grains within gypsum and the surrounding wall rock (Fig. 3F). A previous  
139 study by Martin et al. (2021) demonstrated that the pyrite-gypsum relationships preserved at Mala are  
140 analogous to those observed in actively forming SMS deposits and reflect primary hydrothermal processes  
141 and are not the result of supergene weathering during uplift and exposure.

## 142 Methods

### 143 Mineral Chemistry

144 Laser ablation ICP-MS was used to determine *in situ* trace element concentrations in pyrite. Spot analyses  
145 (n=143) were performed on 10 representative polished blocks. Analyte masses used were <sup>57</sup>Fe, <sup>65</sup>Cu, <sup>59</sup>Co,



146 <sup>66</sup>Zn, <sup>75</sup>As, <sup>77</sup>Se, <sup>109</sup>Ag, <sup>111</sup>Cd, <sup>121</sup>Sb, <sup>125</sup>Te, <sup>185</sup>Re, <sup>189</sup>Os, <sup>193</sup>Ir, <sup>195</sup>Pt, <sup>197</sup>Au <sup>206</sup>Pb and <sup>209</sup>Bi (Table S1, ESM).  
147 Data were collected using a New Wave Research UP213 laser coupled to a Thermo iCAP RQ-ICP-MS at  
148 Cardiff University, UK. Samples were analysed in time-resolved analysis mode with a nominal spot  
149 diameter of 55 µm at a frequency of 10 Hz. Each analysis lasted 40 s and a gas blank was measured for 20  
150 s prior to each analysis. Data correction and the subtraction of gas blanks was performed using Thermo  
151 Qtegra software. External calibration was performed on a series of synthetic NiFeS standards (see Prichard  
152 et al. 2013; Smith et al. 2016) and the reproducibility of analyses was monitored through the repeat analysis  
153 of UQAC FeS-1. The repeat analysis of UQAC FeS-1 yielded a relative standard deviation (RSD) of <10%  
154 for Fe, Co, Ni, As, Ru, Rh, Pd, Ag, Re, Os, Ir, Pt, Au and Bi, <15% for Cu, Se, Sb and Te and <20% for  
155 Zn and Pb. The RSD for Cd was 24% (Table S2, ESM). Detection limits for all elements analysed are  
156 available in ESM Table S2. Sulfur-33 was used as an internal standard for all analyses and a stoichiometric  
157 concentration of 53.5 wt.% sulfur was used that is within error of the measured average sulfur concentration  
158 for pyrite from Troodos VMS deposits (Martin et al. 2019).

159

## 160 Sulfur Isotope analysis

161 Secondary ion mass spectrometry microanalysis was used to determine the sulfur isotope composition  
162 ( $\delta^{34}\text{S}$ ) of pyrite. Analysis was undertaken on the same samples analysed via LA-ICP-MS. Epoxy mounted  
163 polished blocks (n=6) were first coated with 300Å of Au and were analysed using a Cameca IMS 4f SIMS  
164 at the MAF-IIC Microanalysis Facility at Memorial University of Newfoundland following the procedures  
165 detailed in Brueckner et al. (2015) and Lode et al. (2017). Systematic analysis of points across pyrite grains  
166 was performed proximal to LA-ICP-MS ablation pits to determine variation and correlation between  $\delta^{34}\text{S}$   
167 values and trace element concentrations. The sample was bombarded with a primary ion beam of 350-750  
168 pA of  $\text{Cs}^+$ , accelerated through a potential of 10 keV and focused into a 5-15 µm diameter spot. The duration  
169 of each analyses was 16.3 minutes including 2 minutes of pre-sputtering. To discriminate between  $^{33}\text{SH}^-$   
170 (and  $^{32}\text{SH}_2^-$ ) from  $^{34}\text{S}^-$  the instrument was operated with a medium contrast aperture (150 µm), with entrance



171 and exit slits paired to give flat topped peaks at a mass resolving power of 2975 (10% peak height definition;  
172 Brueckner et al. 2015). Negatively charged sputtered secondary ions were accelerated into the mass  
173 spectrometer using a potential of +4.5 keV. To exclude sulfur contamination from the sample surface the  
174 spot was pre-sputtered for 120 s with a 15  $\mu\text{m}$  square rastered beam prior to analysis. Reproducibility based  
175 on the repeat analysis of standard reference material pyrite-UL9 ( $\delta^{34}\text{S}= 16.3\%$ ) and KH87 ( $\delta^{34}\text{S}= 0.4\%$ ),  
176 is typically better than  $\pm 0.4\%$  ( $1\sigma$ ) (Table S3, ESM). All analyses are reported in standard notation ( $\%$ )  
177 relative to Vienna-Canyon Diablo Troilite (V-CDT).

178

## 179 Results

### 180 Sample characterization

181 Samples in this study were collected from the exposed Mala VMS mound (Fig. 2A and Fig. S1, ESM). We  
182 subdivide pyrite samples based on texture into massive, dendritic, colloform, granular, and disseminated  
183 varieties (Fig. 3). Massive pyrite occurs in discrete meter scale pods consisting of coarse grained (mm to  
184 cm) aggregates of euhedral grains (Fig. 2C and 3A and B). Multiple pyrite generations occur as overgrowths  
185 within massive pyrite samples and can be delineated by inclusion-rich zones at the grain margin (Fig. 3A).  
186 Within massive pyrite, dendritic horizons were common but were not analysed in this study (Fig. 3B and  
187 C). Colloform pyrite is rare, occurring spatially associated with granular horizons (Fig. 3D). Granular  
188 massive pyrite contains anhedral aggregates of highly resorbed and often spherical pyrite in a pyrite matrix  
189 (Fig. 3E). Disseminated pyrite grains are commonly euhedral and vary in size from  $<1$  mm to  $>2$  cm, and  
190 occur within gypsum horizons as well as within the volcanic rocks that surround the massive sulfide mound  
191 (Fig. 2D and 3F).

### 192 Trace element geochemistry

193 To assess trace metal enrichment profiles, results are grouped based on pyrite texture, and, for disseminated  
194 grains, the location of the analytical point in relation to the core or rim of the individual mineral grain that

195 was analyzed. The division between core and rim is arbitrary and depends on the number of analyses  
196 performed within an individual pyrite grain, which in turn reflects the size of the pyrite grain (Table S1,  
197 ESM).

198 Colloform pyrite (n=15) contains the highest median concentrations of Au, Pb and Re at 0.13, 9.8 and 0.17  
199 ppm, respectively. All Ni and Cd analyses are below the detection limit, as are the majority of Cu, Zn and  
200 Co (Table 1; Fig. 4A). The concentration of Se is relatively homogenous ranging from 190 to 302 ppm with  
201 a median concentration of 245 ppm (n=15) (Fig. 4B, Table 1). The total measured trace metal content for  
202 colloform pyrite is 371 ppm (Fig. 4D). A strong positive correlation is noted between Au and Ag ( $R^2=0.95$ ),  
203 and a moderate positive correlation between Pb and Ag ( $R^2=0.72$ ), Te and Au ( $R^2=0.56$ ) and Te and Bi ( $R^2$   
204  $=0.52$ ).

205 Granular pyrite (n=10) is depleted in most trace metals relative to other pyrite textures considered here. All  
206 analyses for Ni, Ag, Zn, Cd, Re and Pb are below detection limit as are the majority of analyses for Au, Bi,  
207 Cu and Sb (Table 1). Cobalt and Te are notably enriched relative to colloform pyrite with median  
208 concentrations of 17.9 and 5.9 ppm, respectively (n=10; Fig. 4A; Table 1). As observed in colloform pyrite,  
209 the concentration of Se is relatively homogenous, ranging from 5 to 31 ppm, with a median concentration  
210 of 6.4 ppm (n=10) (Fig. 4B, Table 1). With the exception of a moderate correlation between As and Se ( $R^2=$   
211  $0.63$ ) no notable correlations exist. Granular pyrite contains the lowest measured total trace metal content  
212 at 198 ppm (Fig. 4D).

213 Trace metal enrichment profiles in massive pyrite (n=40) are highly variable between samples. For  
214 example, sample MAL 17 is enriched in Cu with a median concentration of 0.04 wt.% with a range of  
215 between 0.01 to 0.11 wt.% (n=10) but is relatively depleted in Se with a median concentration of 61 ppm  
216 (n=10) (Fig. 4A, Table 1). Across all massive samples, Se exhibits the most variation, ranging from 30 to  
217 1253 ppm with a median concentration of 178 ppm (n=40) (Fig. 4B). With the exception of one point, all  
218 analyses for Ni and Cd were below the detection limit (Table 1). Massive pyrite contains the second highest

219 total measured metal content at 566 ppm (Fig. 4D). A weak correlation is noted between Te and Se ( $R^2 =$   
220 0.38; Fig. 4B).

221 Grains of disseminated pyrite within gypsum (n=78) contain the highest concentration of Se, Te, As and Bi  
222 relative to all other pyrite textures (Fig. 4A-C, Table 1). Trace metal concentrations are highly variable  
223 within and between individual samples relative to other pyrite textures analysed in this study. For example,  
224 Se concentrations range from 18 to 3261 ppm with a median concentration of 645 ppm (n=78). Similar  
225 variability is also noted for Co, As and Te (Table 1; Fig. 4B-C). Sample MAL 05 is notably enriched in Se  
226 and Te relative to all other samples with median concentrations of 1668 and 16.4 ppm, respectively (n=14).  
227 Disseminated grains have the highest total measured metal content at 981 ppm (Fig. 4D); largely consisting  
228 of Se and Cu. Disseminated pyrite grains are sub-divided further based on the location of the analytical  
229 point relative to the margin of the pyrite grain to assess metal enrichment trends across individual grains  
230 (Fig. 5). With the exception of Co and Cu, that are enriched at the margin of grains (n=43), pyrite cores  
231 exhibit a minor enrichment in As, Se, Te and Au relative the grain margins (n=35; Fig. 5).

## 232 Sulfur isotopes

233 Secondary ion mass spectrometry analysis was performed on representative samples of colloform (n=6),  
234 granular (n=2), massive (n=9) and disseminated (n=14) textured pyrite (Fig. 6, Table S3, ESM). The median  
235  $\delta^{34}\text{S}$  value for all samples is -1.2‰ (n=31) with a range of 24.6‰. Granular pyrite exhibits the lightest  
236 median sulfur isotopic composition with two analyses yielding  $\delta^{34}\text{S}$  values of -10.5‰ and -4.7‰. Colloform  
237 pyrite consistently exhibits  $\delta^{34}\text{S}$  values <0‰ ranging from -3.8 to -0.1‰ with a median of -2.2‰ (n=6)  
238 (Fig. 6). The sulfur isotopic composition of massive pyrite is highly variable, ranging from -17.1‰ to 7.5‰  
239 with a median composition of -1.8‰ (n=9).

240 To assess intra-grain variation in sulfur isotopic composition of disseminated pyrite, transects of analytical  
241 points were analysed across different pyrite grains (Fig. 7). The same grains were then etched with NaClO  
242 for 90 s to reveal any chemical zonation. A significant amount of variability is recorded in a single pyrite

243 grain, for example MAL 05 where  $\delta^{34}\text{S}$  values range from 2.5‰ to -10.9‰ (sub-grain SG1) with a median  
244 of 2.0‰ (n=4, Fig. 7A). There is no systematic relationship between  $\delta^{34}\text{S}$  values and the location of the  
245 analysis with respect to the core or rim of the grain, for example, low values do not only occur at the margin  
246 of the grain. This is best illustrated in sample MAL 05, an aggregate of three pyrite grains disseminated  
247 within gypsum where opposing edges of the pyrite sub-grain SG1 have  $\delta^{34}\text{S}$  values of -10.9‰ and 2.5‰,  
248 respectively (Figure 7A). Individual pyrite grains that are located within the same region of the VMS mound  
249 (Fig. 2 and Fig. S1, ESM) also exhibit notable variation, for example two grains from sample MAL 11 (Fig  
250 7B and C) that have different median  $\delta^{34}\text{S}$  values of -0.9‰ and 0.9‰, respectively (n=7). Again, there is  
251 no systematic pattern of enrichment from the grain core to rim within these grains.

## 252 Discussion

### 253 Mound-scale trace element systematics

254 The trace metal content and ratio of metals in pyrite can be used as a proxy for the past physical and  
255 chemical conditions of hydrothermal fluids (e.g., temperature, pH,  $f\text{O}_2$  and  $f\text{S}_2$ ) (Butler and Nesbitt 1999;  
256 Hannington et al. 2005; Maslennikov et al. 2009; Genna and Gaboury 2015; Wohlgemuth-Ueberwasser et  
257 al. 2015; Keith et al. 2016b; Monecke et al. 2016; Grant et al. 2018; Wang et al. 2018). Thus, variations in  
258 trace metal enrichment profiles in pyrite in VMS deposits reflect changes in the physicochemistry of fluids  
259 and the flux of metals and fluid entering the VMS deposit during growth of the VMS mound. At the mound  
260 scale (~10s of m) steep temperature gradients occur due to variations in the relative amounts of seawater  
261 ingress and hydrothermal fluid influx with depth within the mound. Increasing temperatures within the  
262 mound lead to the dissolution, recrystallization and remobilization of metals associated with lower  
263 temperature sulfide minerals (e.g., Zn, Au, Ag, As, Pb, Sb) from the mound interior to the cooler margin of  
264 the mound during zone refining (Eldridge et al. 1983; Hannington et al. 1986; Petersen et al. 2000; Galley  
265 et al. 2007). This process is preserved in active SMS deposits as systematic variations in trace metal  
266 enrichment profiles between different pyrite textures, such as colloform pyrite that forms near the seawater

267 interface that is enriched in elements that are associated with low temperature sulfide minerals or those  
268 sourced from seawater (e.g., Mo, Tl, Pb; Grant et al. 2018). We note the same systematic variation in the  
269 distribution of trace metals between different pyrite textures at the Mala VMS deposit.

270 Colloform pyrite occurs in active SMS deposits towards the margin of the sulfide mound or during the early  
271 stage of chimney growth in environments where seawater ingress is high and fluid temperatures are lower  
272 producing non-equilibrium conditions (Maslennikov et al. 2009, 2017; Melekestseva et al. 2014;  
273 Wohlgemuth-Ueberwasser et al. 2015; Keith et al. 2016a,b; Grant et al. 2018). Colloform pyrite from Mala  
274 is enriched in Au and Pb relative to all other pyrite and contains the lowest median concentration of Co, Cu  
275 and Te, with all Ni analyses below detection limit, indicating it formed at lower fluid temperatures. At these  
276 low concentrations, both Au and Pb are likely incorporated into the pyrite structure as a lattice bound  
277 substitution, whilst at higher concentrations inclusions may occur (Huston et al. 1995; Cook et al. 2009).  
278 This trace metal enrichment profile is similar to those reported in colloform pyrite from black smoker  
279 chimneys of Urals VMS deposits that are enriched in Au, Ag, Pb and elements derived from seawater such  
280 as Mo and Tl that were not analysed in this study (Maslennikov et al. 2009) or colloform pyrite from  
281 PACMANUS that is enriched in Au and As but depleted in Te and Se relative to massive pyrite  
282 (Wohlgemuth-Ueberwasser et al. 2015). A depletion in Co and Te, which are enriched in high-temperature  
283 pyrite varieties (e.g., massive pyrite) in active SMS deposits, further supports a low temperature origin for  
284 colloform pyrite at Mala (Wohlgemuth-Ueberwasser et al. 2015; Monecke et al. 2016; Grant et al. 2018).  
285 The trace element enrichment profile in colloform pyrite at Mala is comparable to colloform pyrite from  
286 the actively forming TAG SMS deposit located at the Mid-Atlantic Ridge (Grant et al. 2018) and from  
287 colloform pyrite at the Skouriotissa VMS deposit (Keith et al. 2016a). Primarily, this trace metal enrichment  
288 profile reflects the location of colloform pyrite at shallow depths within the VMS mound in close proximity  
289 to the seawater interface, and its formation under lower fluid temperatures generated by increased amounts  
290 of seawater mixing relative to massive pyrite at deeper stratigraphic levels in the VMS mound (Monecke  
291 et al. 2016).

292 Mala colloform pyrite is strongly enriched in Se (Fig. 4) relative to concentrations reported for colloform  
293 pyrite at the Skouriotissa VMS deposit (Troodos) that average  $12 \pm 10$  ppm ( $1\sigma$ ,  $n=52$ ; Keith et al. 2016a),  
294 black smoker chimneys from Urals VMS deposits that average  $9 \pm 5$  ppm ( $1\sigma$ ,  $n=8$ ; Maslennikov et al. 2009),  
295 concentrations of  $<4.5$  ppm at the Semenov vent field (Melekestseva et al. 2014), and the TAG and  
296 PACMUS (Roman Ruins) deposits where colloform pyrite did not contain any detectable Se (Wohlgemuth-  
297 Ueberwasser et al. 2015; Grant et al. 2018). This concentration is also notably higher than that typically  
298 recorded in colloform pyrite in other Troodos VMS deposits where the median concentration is 49 ppm  
299 (Martin et al. 2019, 2020). Several studies indicate that Se is preferentially enriched in pyrite that formed  
300 in high-temperature regions of the VMS mound or the interior conduit of black smoker chimneys, indicating  
301 an affinity for high temperature fluids (Butler and Nesbitt, 1999; Maslennikov et al. 2009; Revan et al.  
302 2014; Grant et al. 2018). However, at Mala Se is also enriched in pyrite that is interpreted to have formed  
303 at lower temperatures, and we suggest that the enrichment of Se in colloform pyrite is a consequence of an  
304 increased magmatic volatile influx.

305 Granular textured massive pyrite occurs towards the margin of the sulfide mound and forms through the  
306 collapse and physical reworking of sulfide fragments during the growth of the VMS deposit (Humphris et  
307 al. 1995; Petersen et al. 2000). Granular pyrite contains the lowest total measured trace metal content but  
308 is relatively enriched in Te compared to other pyrite varieties (Table 1; Fig. 4A). We suggest that metal  
309 enrichment profiles in granular pyrite reflect the remobilization and subsequent loss of some metals during  
310 zone refining and oxidization of primary massive pyrite at low temperatures ( $<100^\circ\text{C}$ ) at or near the seafloor  
311 towards the periphery of the VMS mound (Herzig et al. 1991; Hannington et al. 1998; Fallon et al. 2017;  
312 Murton et al. 2019). Assuming that massive pyrite samples represent the primary trace metal content of  
313 granular samples prior to reworking, then all elements have been depleted during reworking with the  
314 exception of Te. The enrichment of Te, which is readily mobilized under oxidizing and low temperature  
315 fluid conditions (e.g., McPhail 1995), possibly indicates that the granular sample analysed was initially  
316 enriched in Te prior to reworking.

317 Massive pyrite at Mala occurs as discrete pods throughout the sulfide mound. The trace metal composition  
318 is highly variable depending on the individual sample analysed (Table S1 and Fig. S1, ESM). Fluid flow  
319 regimes evolve with time in response to permeability fluctuations related to the collapse and occlusion of  
320 permeability pathways, leading to the disruption of high-temperature fluid flow pathways within the VMS  
321 mound (e.g., Tivey et al. 1995; You and Bickle 1998; Tivey 2007). These local-scale fluctuations (cm to  
322 m's) in fluid flow led to changes in temperature and the remobilization of metals stable at low temperatures  
323 from areas proximal to zones of high temperature fluid flow ( $>350^{\circ}\text{C}$ ) within the mound, leading to highly  
324 heterogeneous trace metal enrichment profiles between different massive pyrite samples. For example,  
325 samples located proximal to high temperature ( $>350^{\circ}\text{C}$ ) fluid pathways (e.g., MAL 14) are relatively  
326 enriched in Se, Co and Te compared with samples that have experienced zone refining during fluid  
327 overprinting by later cooler fluids ( $<350^{\circ}\text{C}$ ) (e.g., MAL 17). Hence, such large variations in trace metal  
328 concentrations between massive pyrite samples reflects the dynamic nature of fluid flow within the VMS  
329 mound. Alternatively, pyrite that contains low total trace metal concentrations may have been affected by  
330 a higher degree of zone refining leading to the localised leaching and remobilization of most trace metals,  
331 even those associated with high temperature assemblages as suggested for the Kokkinopezula VMS deposit  
332 in Troodos (Hannington et al. 1998). However, high degrees of zone refining are considered to occur in  
333 mature VMS deposits, whereas the Mala deposit is suggested to represent an immature system based on the  
334 elevated concentration of magmatic volatile elements and low sulfur isotope values (Martin et al. 2021)  
335 and, therefore, it is unlikely that enough time has elapsed to reach the high degree of zone refining.

336 Disseminated pyrite occurs as euhedral grains within gypsum (Fig. 2D) and is strongly enriched in Se  
337 compared to all other pyrite textures (Fig. 5). This enrichment in Se is most likely a function of the  
338 preferential partitioning of Se into disseminated pyrite grains relative to the surrounding gypsum/anhydrite  
339 matrix (Yamamoto 1976; Huston et al. 1995). Alternatively, the enrichment of Se could indicate that  
340 disseminated pyrite formed under lower fluid temperatures, assuming that Se is transported as  $\text{H}_2\text{Se}$  in the  
341 hydrothermal fluid, as thermodynamic models for Se in pyrite predict that it is preferentially enriched at



342 lower temperatures (150°C) and more oxidizing conditions ( $\Sigma\text{SO}_4 > \Sigma\text{H}_2\text{S}$ ; Huston et al. 1995). However,  
343 observations from the active TAG deposit indicate that anhydrite-rich zones, that are analogous to gypsum-  
344 rich zones at Mala where disseminated pyrite occurs, typically form at temperatures  $>350^\circ\text{C}$  (Edmond et  
345 al. 1995; Grant et al. 2018; Petersen et al. 2000). Furthermore, pyrite grains appear euhedral with no  
346 hematite or magnetite that would indicate more oxidized fluids. Thus, there is no evidence supporting the  
347 formation of disseminated pyrite from more oxidized or low-temperature ( $\sim 150^\circ\text{C}$ ) fluids at Mala that are  
348 favorable for the incorporation of Se in pyrite (Yamamoto 1976; Huston et al. 1995).

349 As observed in massive pyrite samples, notable variation exists between individual disseminated samples  
350 (Fig. 8). We use the Te and Se content of pyrite as proxies for magmatic volatile influx as these elements  
351 are enriched in VMS deposits in volatile-rich subduction influenced environments (Keith et al. 2016b) and  
352 Co and As as indicators of high and low temperature fluids, respectively (Grant et al. 2018) (Fig. 8).  
353 Samples MAL 18 and MAL 05 are located in the upper mound region, whilst MAL 04 and MAL 11 are  
354 located in the lower mound (Fig. 2A). Based on studies of the active TAG mound, spatial trends in the trace  
355 metal content of pyrite exists with, for example, Ni, Co and Se enrichment in high-temperature stockwork  
356 zones and As, Pb, Zn and Ag enrichment in lower temperature massive pyrite (Grant et al. 2018). Sample  
357 MAL 05 contains notably higher Se and Te concentrations relative to all other grains, and is depleted in Co  
358 and enriched in As, indicating that it formed at low temperatures. In contrast, sample MAL 18, which also  
359 formed in the upper mound area, is relatively depleted in Se, Te and As but is strongly enriched in Co,  
360 indicating that it formed from high temperature fluids ( $>350^\circ\text{C}$ ; Metz and Trefry 2000; Keith et al. 2016a;  
361 Grant et al. 2018) (Fig. 8). Some samples (e.g., MAL 04) from the lower mound are depleted in As, Co, Te  
362 and Se relative to other samples, possibly providing evidence for high degrees of zone refining (Hannington  
363 et al. 1998). The trace metal enrichment profile in samples from the lower mound are highly variable with  
364 some analyses strongly enriched in Te, Se, Co and As, indicating a change in fluid temperature and/or  
365 magmatic volatile influx as the pyrite grain grew. The sporadic variation in trace metal concentrations  
366 within individual disseminated pyrite grains indicates the influence of dynamic fluid flow regimes within

367 the VMS mound that leads to strong and transient physicochemical gradients localised over cm to m scales.  
368 Hence, our data indicate that the well-established zone-refining model that is modelled on the active TAG  
369 deposit (Humphris et al. 1995; Grant et al. 2018) is more complex when considering the distribution of  
370 trace metals, especially when accounting for the distribution of metals over individual mineral grains. This  
371 notwithstanding, there are obvious similarities between actively forming SMS deposits and the zonation of  
372 metals in black smoker chimneys with the ancient Mala VMS deposit, suggesting that processes that control  
373 the mound scale distribution and cycling of trace metals are broadly analogous between the two and did not  
374 change since the Cretaceous.

### 375 Sulfur isotope systematics

376 Sulfur isotope analysis of sulfide minerals, such as pyrite, in VMS deposits can be used to discriminate  
377 contributions from isotopically-distinct reservoirs of sulfur in hydrothermal fluids, such as sulfur leached  
378 from oceanic crust, seawater sulfate, and, SO<sub>2</sub> degassing from shallow magma chambers (Lüders et al.  
379 2001; Hannington et al. 2005; Ono et al. 2007; de Ronde et al. 2011; Keith et al. 2016a; Martin et al. 2020;  
380 LaFlamme et al. 2021). The two primary sources of sulfur in Troodos VMS deposits are the bulk Troodos  
381 crust that has a sulfur isotope composition of 1 to 0‰ (Alt 1994), Cretaceous seawater sulfate at  $\delta^{34}\text{S} = 18$   
382 to 19‰ (Kampschulte and Strauss 2004), and at the Mala VMS deposit, the disproportionation of SO<sub>2</sub>  
383 (Martin et al. 2021). The mixing of sulfur sourced from TSR of seawater and the leaching of primary  
384 igneous sulfur/sulfide from host rocks (Woodruff and Shanks 1988; Shanks 2001) lead to an average  $\delta^{34}\text{S}$   
385 value in pyrite of  $4.6 \pm 2.8\%$  ( $1\sigma$ ,  $n=160$ ), indicating that, on average, ~34% of sulfur is sourced from TSR  
386 during VMS deposit formation in Troodos (Martin et al. 2020). The Skouriotissa and Sha, and most notably  
387 the Mala VMS deposits, contain pyrite with a sulfur isotopic composition that is less than <0‰. Previously,  
388 the low  $\delta^{34}\text{S}$  values in pyrite have been attributed to the disproportion of SO<sub>2</sub> during the degassing of  
389 volatiles from a shallow magma chamber (Keith et al. 2016a; Martin et al. 2020). At Mala,  
390 disproportionation generates sulfate with a sulfur isotopic composition of 14.5‰ in gypsum ( $n=26$ ), and  
391 pyrite that is depleted in <sup>34</sup>S on average by -4.3‰ ( $n=28$ ) (Martin et al. 2021). Bacterial sulfate reduction

392 of seawater at low temperatures (<120°C) can also form negative  $\delta^{34}\text{S}$  values in pyrite as low as -22.2‰ in  
393 altered oceanic crust in Troodos, such as those found in pyrite veins in the pillow lavas, indicating that BSR  
394 occurred distally to high-temperature VMS deposits in the shallow lava stratigraphy (Alt 1994; Pedersen et  
395 al. 2017).

396 The *in situ* analysis of different pyrite textures indicates that the source of sulfur in the Mala VMS deposit  
397 was not constant and evolved with time, leading to variations in  $\delta^{34}\text{S}$  values across individual pyrite grains.  
398 Variation in  $\delta^{34}\text{S}$  values between pyrite textures relates to mound-scale fluid flow that is directly influenced  
399 by the location of specific pyrite samples within the mound that in turn influences pyrite texture (e.g.,  
400 colloform vs. massive samples). Similar variations are reported across black smoker chimneys where  
401 intense gradients in temperature and fluid mixing occur within the chimney wall (Haymon 1983; Crowe  
402 and Valley 1992). For example,  $\delta^{34}\text{S}$  varies from 2.1 to 6.4‰ in pyrite from the interior to exterior chimney  
403 wall, respectively, in a black smoker chimney from 1-2°S on the EPR (Meng et al. 2020). Given the large  
404 range in  $\delta^{34}\text{S}$  values of pyrite at Mala, from -17.1‰ to 7.5‰, we suggest four processes that account for  
405 the observed variation in the sulfur isotope composition of pyrite: i) TSR of seawater (18 to 19‰), ii) the  
406 leaching of igneous sulfide (0 to 1‰), iii) the disproportionation of degassing  $\text{SO}_2$  (0 to 1‰) and, iv) BSR.  
407 Firstly, considering variation in sulfur isotope composition with pyrite texture, previous studies note a  
408 systematic relationship between stratigraphic depth and  $\delta^{34}\text{S}$  values in pyrite from the Skouriotissa VMS  
409 deposit (Keith et al. 2016a), where enrichment of  $^{34}\text{S}$  in shallow euhedral and colloform textured pyrite  
410 leads to  $\delta^{34}\text{S}$  values of 4.7‰ and 4.9‰, respectively (n=4, Keith et al. 2016a). This variation is attributed  
411 to the increased proportion of sulfur that is incorporated from TSR of Cretaceous seawater in regions of the  
412 VMS mound near the seawater interface. In contrast, deep, stockwork pyrite has a  $\delta^{34}\text{S}$  value of -1.4‰  
413 indicating lesser amounts of TSR and leaching of igneous sulfur/sulfide and an increased amount of sulfur  
414 sourced from the disproportionation of degassing  $\text{SO}_2$ , producing a sulfur isotope composition in pyrite that  
415 is less than the Troodos magmatic mean (0-1‰; Alt 1994) (Keith et al. 2016a). Data presented in this study  
416 for the Mala VMS deposit has a range of 24.6‰ (n=31), notably more variable than Skouriotissa with a

417 range of 7.8‰ (n=29; Keith et al. 2016a; Martin et al. 2020), with no systematic variation between  $\delta^{34}\text{S}$   
418 values and pyrite texture at Mala (Fig. 6 and 9). Instead, 18 of the 31 analyses across disseminated, granular,  
419 colloform and massive textured pyrite contain  $\delta^{34}\text{S}$  values of less than the Troodos magmatic mean of  $\sim 0\%$   
420 (Fig. 9; Alt 1994). This supports previous interpretations that have been proposed for the Mala VMS deposit  
421 that indicates sulfur was sourced from a mixture of  $\text{SO}_2$  disproportionation, TSR and leaching of igneous  
422 sulfur/sulfide. However, the low  $\delta^{34}\text{S}$  values measured in massive pyrite (down to  $-17.1\%$ ), which are much  
423 lower than any values previously reported, could be produced either via the low temperature  
424 disproportionation of  $\text{SO}_2$  or during BSR of Cretaceous seawater. Based on the expected fractionation  
425 factors between  $\text{SO}_2$  and pyrite (after Sakai 1968),  $\text{SO}_2$  disproportionation would have had to occur at a  
426 temperature of  $\sim 120^\circ\text{C}$  to account for the measured depletion in  $^{34}\text{S}$  to  $-17.1\%$ , assuming a starting  $\text{SO}_2$   
427 composition of  $0\%$ . Alternatively, at low temperatures ( $<120^\circ\text{C}$ ) BSR of seawater sulfate can generate  
428 large depletions in  $^{34}\text{S}$  up to  $-38.9\%$  in pyrite (Habicht and Canfield 1997; Wortmann et al. 2001; Farquhar  
429 et al. 2003; Rouxel et al. 2008; Alt and Shanks 2011; Nozaki et al. 2020).

430 In active seafloor hydrothermal systems evidence for both the low temperature disproportionation of  $\text{SO}_2$   
431 and BSR exist. Negative  $\delta^{34}\text{S}$  values attributed to the disproportionation of  $\text{SO}_2$  down to  $-17.5\%$  are found in  
432 active seafloor hydrothermal systems that experience an increased influx of magmatic volatiles, such as  
433 Conical seamount, Papa New Guinea (Gemmell et al. 2004), however typical median values are less  
434 extreme, for example the median  $\delta^{34}\text{S}$  values at Conical seamount are  $-1.2\%$  (n=66) (Petersen et al. 2002;  
435 Gemmell et al. 2004) at Hine Hina, Valu Fa Ridge, Lau Basin,  $-4.5\%$  (n=12) (Herzig et al. 1998), at  
436 Brothers volcano, Kermadec arc,  $-2.9\%$  (n=87) (Kermadec arc; de Ronde et al. 2005, 2011) and  $-5.6\%$   
437 (n=13) at SuSu Knolls, Manus back-arc basin (Kim et al. 2004), indicating that sulfur was sourced from a  
438 combination of  $\text{SO}_2$  disproportionation, TSR and leaching of igneous sulfur/sulfide.

439 Evidence of BSR has also been suggested as an important processes in the Agrokipia B VMS deposit  
440 (Troodos) where multiple sulfur isotopes ( $\Delta^{33}\text{S}$ ) indicate re-working of sulfide minerals in the upper part of  
441 the VMS mound by microbes was an important but localised process (Pedersen et al. 2017). In lower

442 temperature regions of the Troodos stratigraphy, similar  $\delta^{34}\text{S}$  values of -17.2‰ and as low as -22.2‰ (Alt  
443 1994; Pedersen et al. 2017) have been reported for vein pyrite from the upper lava stratigraphy where the  
444 occurrence of analcime, natrolite and phillipsite indicate the presence of low temperature fluids (<100°C;  
445 Gass and Smewing 1973) where BSR could occur.

446 The negative  $\delta^{34}\text{S}$  signature, down to -17.1‰, with a median composition of -13.7‰ (n=3) for the massive  
447 sulfide sample at Mala, is somewhat enigmatic as both disproportionation of  $\text{SO}_2$  and BSR require low fluid  
448 temperatures <120°C to explain the observed  $\delta^{34}\text{S}$  signature. Fractionation factors between  $\text{SO}_2$  and pyrite  
449 (Sakai, 1968), using an initial value of 0‰, would have had to occur at a temperature of 187°C to explain  
450 the median sulfur isotopic composition in pyrite of -13.7‰; assuming that  $\text{SO}_2$  disproportionation was the  
451 only source of sulfur (i.e. a closed system), which as shown in previous studies is not the case (Ono et al.  
452 2007).

453 Combining trace element geochemistry and sulfur isotope data, we suggest that the  $\delta^{34}\text{S}$  signature is best  
454 explained by BSR of seawater. Disproportionation of  $\text{SO}_2$  that indicates magmatic volatile influx is, at the  
455 mound scale, commonly associated with increased concentrations of Se, Te and Au in the Mala VMS  
456 deposit (Martin et al. 2021); however this is not the case in massive pyrite sample MAL 17, that is depleted  
457 in Te, Se and Au compared to all other massive pyrite samples. Furthermore, MAL 17 has a median Co  
458 concentration of 8.4 ppm (n=10), compared to 38.7 ppm for all massive samples (n=40), further supporting  
459 its formation from relatively low temperature fluids (<350°C) (Keith et al. 2016a,b; Monecke et al. 2016;  
460 Grant et al. 2018). The relative depletion in Te, Se and Au is not consistent with its formation during  
461 magmatic degassing, indicating it most likely formed during the BSR of seawater. This is further supported  
462 by the location of the sample on the western margin of the VMS mound (Fig. 2A), and assuming that the  
463 mound morphology preserved today is representative of how the Mala VMS deposit formed at the  
464 Cretaceous seafloor, the sample is located near the seawater interface where seawater ingress is high and  
465 the fluid temperature is expected to be low, possibly <120°C (cf. Pedersen et al. 2017).

466 The sulfur isotopic composition of colloform textured pyrite at Mala has a median  $\delta^{34}\text{S}$  value of -2.2‰  
467 (n=6; Fig. 4). This is significantly lower than the median  $\delta^{34}\text{S}$  value recorded in colloform pyrite at the  
468 Skouriotissa VMS deposit of 4.9‰ (n=2; Keith et al. 2016a), the Ice VMS deposit (Yukon, Canada) at  
469 5.0‰ (n=8; McDonald et al. 2018), and the Ezuri VMS deposit (Hokuroko, Japan) at 4.5‰ (n=16; Barrie  
470 et al. 2009). The positive values found in colloform pyrite in most VMS deposits demonstrate that the  
471 primary source of sulfur is the leaching of igneous basement and TSR of seawater (Ohmoto 1996; Barrie  
472 et al. 2009; Keith et al. 2016a; McDonald et al. 2018). By contrast,  $\delta^{34}\text{S}$  values in colloform pyrite at Mala  
473 are less than the Troodos magmatic mean (0-1‰; Alt 1994) indicating that sulfur was not *only* sourced via  
474 TSR of Cretaceous seawater and the leaching of igneous lithologies, instead indicating that colloform pyrite  
475 formed during the disproportionation of  $\text{SO}_2$ . Using the fractionation between  $\text{SO}_2$  and pyrite (Sakai 1968),  
476 the expected fractionation at 350°C would be 8.6‰. In order to explain the observed fractionation between  
477 the median  $\delta^{34}\text{S}$  value in colloform pyrite (2.2‰) and primary igneous sulfur/sulfide (0‰) the fluid  
478 temperature would have had to be >880°C. As previously established for bulk rock samples, this  
479 temperature is unrealistically high for VMS deposit formation, hence we suggest that the disproportion of  
480  $\text{SO}_2$  occurred at lower fluid temperatures where fractionation between  $\text{SO}_2$  and pyrite is greater and that the  
481 higher than anticipated  $\delta^{34}\text{S}$  values in colloform pyrite reflects the addition of a  $^{34}\text{S}$  enriched source from  
482 both TSR and the leaching of igneous sulfur/sulfide providing an additional source of sulfur in colloform  
483 pyrite.

484 Disseminated pyrite grains exhibit the largest variation in  $\delta^{34}\text{S}$  values with a median of 0.7‰ and a range  
485 of 16.8‰ (n=14). To assess if the pyrite analysed are singular grains or aggregates of sub-grains, etching  
486 was used to reveal any internal variation (Fig. 7). Sample MAL 05 (Fig. 7A) exhibits internal variation  
487 appearing as three different colored sections, indicating it is formed from three sub-grains. In contrast, the  
488 etched surface of MAL 11A and B does not show any notable variation indicating that they are a single  
489 continuous grain (Fig. 7B and C).

490 The sulfur isotopic composition of individual pyrite grains is highly variable across disseminated pyrite  
491 grains with  $\delta^{34}\text{S}$  values ranging from -10.9‰ to 2.5‰ (within a single sub-grain), suggesting that the source  
492 of sulfur changed as the pyrite crystal grew. However, there is no systematic variation in sulfur isotope  
493 composition between the core and rim of the grain (Fig. 7A), and the two analyses located at the margin of  
494 the grain yield  $\delta^{34}\text{S}$  values of 2.5‰ and -10.9‰, respectively. Instead,  $\delta^{34}\text{S}$  values appear to gradually  
495 decrease across the pyrite grain indicating a change in the source of sulfur as the grain grew (Fig. 7A). In  
496 other pyrite grains a more systematic pattern is discernable where the rim of the grain is enriched in  $^{34}\text{S}$   
497 relative to the core (Fig. 7B and C). This variation could be related to either pulsed fluid flow events  
498 (Butterfield et al. 1994, 2011; Jamieson et al. 2013) that generate fluctuations in fluid flux, temperature,  
499 and the chemical and physical (e.g., phase separation) composition of hydrothermal fluids (Lalou et al.  
500 1990, 1998; Butterfield et al. 1994) or local scale variation in mound-scale fluid flow in response to the  
501 collapse and occlusion of permeability pathways during growth of the VMS mound (Klienrock and  
502 Humphris 1996; Humphris et al. 1995; Hannington et al. 1998; Petersen et al. 2000).

503 Pulsed fluid flow events are linked to magmatic intrusions at depth within the oceanic crust that provide a  
504 renewed source of heat that increases the temperature of venting hydrothermal fluid, volatile influx (e.g.,  
505  $\text{H}_2\text{S}$  and  $\text{SO}_2$ ), and the metal content of fluid vented at the seafloor (Von Damm 1990; Von Damm et al.  
506 1995; Butterfield et al. 1997; Andersen et al. 2017). Several studies document temporal variations in total  
507 sulfur concentrations and major anions (e.g.,  $\text{Cl}^-$ ) in hydrothermal vent fluids sampled from active vent sites  
508 demonstrating that the flux of sulfur in VMS deposits varies temporally (Butterfield and Massoth, 1994;  
509 Von Damm et al. 1995; Butterfield et al. 1997, 2011; Von Damm 1995). It does however remain enigmatic  
510 exactly what these variations mean, for example variations in fluid  $\text{H}_2\text{S}$  concentration could also be  
511 produced during the precipitation or dissolution of sulfide minerals below the seafloor (Reed and Palandri  
512 2006) or during the segregation of  $\text{H}_2\text{S}$  into a vapor phase, thus linking these variations to magmatic  
513 intrusion events is challenging (Von Damm et al. 1995; Butterfield et al. 1997). The dating of SMS deposits  
514 ( $^{210}\text{Pb}/\text{Pb}$ ,  $^{230}\text{Th}/^{234}\text{U}$  and  $^{14}\text{C}$ ) also provides evidence of aperiodic fluid flow with apparent pulses of activity  
515 recorded at the active TAG mound every 2,000 to 6,000 years (Lalou et al. 1993; You and Bickle 1998).



516 In Troodos VMS deposits there are no hydrothermal fluids left to sample nor are the deposits young enough  
517 to be dated using radiometric isotope techniques commonly applied to active SMS deposits, however  
518 variation in rare earth element profiles and Sr isotopes ( $^{87}\text{Sr}/^{86}\text{Sr}$ ) in epidote from the sheeted dykes complex  
519 and plagiogranites, that formed during hydrothermal alteration of the oceanic crust indicate the episodic  
520 release of volatiles into the Troodos hydrothermal systems (Fox et al. 2020). If this was the case then  
521 evidence of pulsed magmatic influx may have been recorded on the scale of individual pyrite mineral grains  
522 as variations in across grain sulfur isotope composition (Fig. 7). Following a volcanic event or the liberation  
523 of magmatic volatiles from the roof of an underlying magma chamber during dyking events, as  
524 hypothesized for Troodos (Gillis and Roberts 1999; Fox et al. 2020), the disproportionation of  $\text{SO}_2$  occurs  
525 and progressively decreases with time from the event, reducing the flux of  $\text{SO}_2$  and subsequent  
526 disproportionation in the overlying hydrothermal system, and the primary source of sulfur changes from  
527 one strongly influenced by disproportionation of  $\text{SO}_2$  to one dominated by TSR and leaching of igneous  
528 sulfur/sulfide. This would produce a pronounced shift in the sulfur isotopic composition across individual  
529 pyrite grains from negative  $\delta^{34}\text{S}$  values indicating  $\text{SO}_2$  disproportionation to values  $>0\text{‰}$  that indicate  
530 increasing amounts of sulfur sourced from TSR and the leaching of igneous sulfur/sulfide (e.g., Fig. 7C).  
531 A similar model has been proposed by earlier studies to explain the sporadic preservation of  $\delta^{34}\text{S}$  values  
532 down to  $-5.5\text{‰}$  in the Sha VMS deposit (Martin et al. 2020). The zonation and aperiodic nature of these  
533 fluctuations in sulfur isotope composition across each mineral grain may be linked to the pulsed nature of  
534 fluid flow during VMS deposit formation, however, further high-resolution mineral-scale data including  
535 mapping of individual mineral grains is required to ascertain the true significance and validity of mineral-  
536 scale sulfur isotope data when applied to system scale pulsed ore-forming processes.

### 537 [A comparison between bulk and \*in situ\* sulfur isotope data](#)

538 The sulfur isotope composition of pyrite from the Mala VMS deposit has previously been assessed using  
539 bulk analytical methods on powdered wholerock samples or pure mineral concentrates (Fig. 9). Using bulk  
540 analytical methods, the  $\delta^{34}\text{S}$  values in pyrite range from  $-7.6\text{‰}$  to  $0.1\text{‰}$  with a median value of  $-4.3\text{‰}$

541 (n=28; Martin et al. 2021) (Fig. 9). Using *in situ* sulfur isotope data collected on the same samples, the  
542 sulfur isotope composition of pyrite varies from -17.1‰ to 7.5‰ with a median value of -1.0‰ (n=31);  
543 variation larger than for the same samples using bulk analytical techniques (Fig. 9). When comparing  
544 between whole rock and *in situ* datasets, on average the difference between the same sample analysed by  
545 SIMS and wholerock methods was 4.9‰ (n=6 samples), with some samples, such as MAL 17, exhibiting  
546 a difference of 7.3‰ between methods. This difference between analytical scales indicates that a significant  
547 amount of variability, and therefore changes in sulfur source and by implication metal source are being  
548 overlooked when using bulk analytical methods compared to *in situ* mineral-scale data. This trend is  
549 comparable to those recognized at Axial Seamount where the bulk analysis of pyrite yield a range of 1.1 to  
550 3.9‰ (Hannington and Scott 1988) whilst *in situ* analysis exhibits more variability with a range of 1.2 to  
551 6.9‰ (Crowe and Valley 1992) or at 1-2° N on the East Pacific Rise (EPR) where bulk pyrite analyses have  
552 a range of 3.0 to 5.8‰ (Zeng et al. 2017) versus *in situ* analysis of pyrite that ranges from 1.8 to 7.5‰  
553 (Meng et al. 2019).

554 To illustrate the disparity between analytical scales we highlight two examples of analytical transects across  
555 pyrite grains (n=23 spots, Fig. 10A). Across a coarse-grained (~1 cm) pyrite grain with three sub-grains  
556 that occurs within gypsum  $\delta^{34}\text{S}$  values exhibit the largest intra-sample range from -10.9‰ to 4.9‰ with a  
557 median of 2.0‰ (n=7) (Fig. 10A). Bulk analysis of the same sample yielded  $\delta^{34}\text{S}$  values of -0.5‰ and -  
558 1.2‰ (Martin et al. 2021). The application of *in situ* analytical methods indicates a variable source of sulfur  
559 with values of -10.9‰ indicating dominantly  $\text{SO}_2$  disproportionation and values of 4.5‰ signifying a larger  
560 contribution of sulfur sourced via TSR of seawater and the leaching of igneous sulfur/sulfide (Fig. 9). A  
561 similar difference between analytical methods is evident in all other samples we analysed (Table S3, ESM);  
562 demonstrating that data obtained at different analytical scales (i.e. mineral vs. bulk samples) can change the  
563 resulting interpretation that is reached.

## 564 Can magmatic volatile influx be traced at the mineral-scale?

565 Previous studies have identified an enrichment of Te, Se, Au, Bi, As, Sb, Pb and Hg in SMS deposits that  
566 form in subduction influenced environments relative to MOR hosted hydrothermal systems, indicating a  
567 link between metal enrichment and magmatic volatile degassing (Hannington et al. 1999; de Ronde et al.  
568 2011; Berkenbosch et al. 2012; Layton-Matthews et al. 2013; Wohlgemuth-Ueberwasser et al. 2015; Fuchs  
569 et al. 2019; Martin et al. 2019; Mathieu 2019; Patten et al. 2020). For example, at the Brothers NW Caldera  
570 site (Kermadec arc), a positive correlation exists between decreasing  $\delta^{34}\text{S}$  values (to  $-4.6\text{‰}$  in sphalerite)  
571 and Au concentration, indicating a link between magmatic volatile influx and Au enrichment (de Ronde et  
572 al. 2011). If certain metals were sourced from a magmatic volatile phase in the Mala VMS deposit, then  
573 they would be expected to show increased concentrations at low  $\delta^{34}\text{S}$  values that indicate an increased  
574 magmatic volatile influx associated with  $\text{SO}_2$  disproportionation (e.g., Herzig et al. 1998). As previously  
575 established, sulfur isotopic ratios exhibit notable variation across individual pyrite grains indicating a  
576 variation in sulfur source that we ultimately relate to a variable magmatic volatile influx. If magmatic  
577 volatile influx occurred as aperiodic releases from the plagiogranites in Troodos into the overlying  
578 hydrothermal systems, a coupled relationship between sulfur isotopes and the enrichment of trace metals  
579 that are associated with increased levels of volatile influx (e.g., Te and Se) should exist in pyrite (Fox et al.  
580 2020). However, our data exhibits limited correlation between Te, Se, Au, As and Co and  $\delta^{34}\text{S}$  values  
581 indicating that the primary magmatic signature/zonation in trace metals, if initially present, was rapidly  
582 modified within the VMS mound.

583 Selenium has been widely applied as an indicator of magmatic volatile influx with Se/S ratios in pyrite used  
584 as evidence of an increased magmatic volatile influx in VMS deposits (Yamamoto 1976; Huston et al. 1995;  
585 Hannington et al. 1999; Layton-Matthews et al. 2008, 2013; Martin et al. 2019). The contribution of Se  
586 from a magmatic volatile phase at Mala is largely supported at the deposit scale by negative  $\delta^{34}\text{S}$  values in  
587 pyrite and a moderate positive correlation between Te and Se ( $R^2=0.67$ ); a trend that is not observed in any

588 other Troodos VMS deposit (Martin et al. 2021). However, mineral grain scale observations show that a  
589 more complex relationship exists (Fig. 10 and 11).

590 If the Se content of pyrite is a reliable proxy for magmatic volatile influx at Mala, then a negative correlation  
591 is expected between Se content and  $\delta^{34}\text{S}$  values in pyrite, with high Se contents occurring in the samples  
592 with low  $\delta^{34}\text{S}$  values indicating a coupled relationship (Yamamoto 1976). The Se content of sample MAL  
593 05, a disseminated pyrite grain in gypsum (Fig. 10A) ranges from 839 to 1727 ppm with the highest Se  
594 concentration corresponding to a  $\delta^{34}\text{S}$  value of 2.5‰. The two lowest Se concentrations of 839 and 1273  
595 ppm correspond to the highest  $\delta^{34}\text{S}$  values measured in MAL 05 of 4.9 and 5.9‰, respectively (Fig. 10A).  
596 However, the two lowest  $\delta^{34}\text{S}$  values of -2.0 and -10.9‰ do not correspond to the highest Se content. Thus,  
597 Se content does not accurately track magmatic volatile influx, if this were the case then a strong correlation  
598 between  $\delta^{34}\text{S}$  values and Se concentration would occur, however this is not observed (Fig. 11B).

599 Renewed volatile influx is driven by magmatic intrusions at depth below the seafloor that lead to an increase  
600 in fluid temperatures preceding the intrusive event, for example at 9° 46.5' N on the East Pacific Rise where  
601 vent fluid temperature varied from 403°C directly after the intrusive event to 322°C three years later (Von  
602 Damm et al. 1995). High Co concentrations in pyrite have been suggested to indicate elevated fluid  
603 temperatures (>350°C), therefore Co should be enriched at low  $\delta^{34}\text{S}$  values that precede the intrusive event  
604 (Butterfield et al. 1997; Keith et al. 2016a,b; Grant et al. 2018). Arsenic is expected to exhibit the inverse  
605 trend as it is concentrated in low temperature pyrite (<350°C) and is expected to be enriched at high  $\delta^{34}\text{S}$   
606 values representing periods of low magmatic volatile influx and correspondingly cooler fluids (Monecke et  
607 al. 2016; Grant et al. 2018). Thus, systematic shifts in Te and Se, that indicate renewed volatile influx, and  
608 As and Co that signify changes in fluid temperature should correlate with changes in  $\delta^{34}\text{S}$  values in pyrite  
609 if they are reliable tracers of magmatic volatile influx at the mineral-scale; we assess this relationship in  
610 disseminated pyrite grains at Mala.

611 In sample MAL 05 Co concentration varies from 12 to 23 ppm (Fig. 10A), exhibiting only a minor  
612 correlation ( $R^2=0.3$ ) with  $\delta^{34}\text{S}$  values (Fig. 10A). Arsenic concentrations are more variable than Co ranging

613 from 5 to 145 ppm with the highest concentration corresponding to a  $\delta^{34}\text{S}$  value of -2.0‰, but with no  
614 notable correlation between As and  $\delta^{34}\text{S}$  values ( $R^2=0.02$ ). A similar trend is evident for Te data with an  
615  $R^2$  value of 0.1 (Fig.10 and 11).

616 In other disseminated grains (Fig. 10B; MAL 11A) the highest Se and Co content correspond to the lowest  
617  $\delta^{34}\text{S}$  value of 0.2‰, whilst Te exhibits the inverse trend (Fig. 10B). A similar trend is also discernable in  
618 MAL 11B where the sulfur isotope composition of pyrite exhibits a saw tooth pattern ranging from -2.5‰  
619 to 0.4‰ (Fig. 10C). Selenium and Te concentrations exhibit a moderate correlation with  $\delta^{34}\text{S}$  values with  
620 an  $R^2$  value of 0.6 and 0.3, respectively. Thus, no clear relationship exists between trace metals and sulfur  
621 isotope composition across disseminated pyrite grains at Mala.

622 For all other samples considered in this study, our data indicate that there is no notable correlation between  
623 Te, Se and Co with  $\delta^{34}\text{S}$  values in individual pyrite grains or within the different textures analysed (Fig.  
624 11). The highest measured Se concentration of 3261 ppm corresponds to a  $\delta^{34}\text{S}$  value of 0‰, whilst lower  
625 values of -2.5‰ within the same mineral grain, which suggest an increased magmatic volatile influx  
626 correspond to a Se concentration of 325 ppm (Fig. 11A). We exclude massive pyrite sample MAL 17 from  
627 our interpretation that is influenced by BSR of seawater leading to a low  $\delta^{34}\text{S}$  value in pyrite and notably  
628 lower concentrations of Se, Te and Co relative to massive and disseminated samples (Fig. 11).

629 Our investigation indicates that variations in Te, Se, Co and As concentrations at the mineral-scale cannot  
630 be linked to variations in magmatic volatile influx at the Mala VMS deposit (Fig. 12). The lack of  
631 correlation between  $\delta^{34}\text{S}$  values and Te, Se, Co and As in the Mala VMS deposit probably reflects the  
632 localized remobilization of trace elements during zone refining related to fluctuations in mound scale fluid  
633 flow related to the collapse and occlusion of fluid pathways during the growth of the mound that leads to  
634 localised zone refining of trace metals in pyrite (Fig. 12). Any initial zonation of trace metals in pyrite  
635 related to the influx of magmatic volatiles is overprinted by later fluid flow that led to the mobilization of  
636 trace metals but does not alter the original sulfur isotope composition of <0‰ related to magmatic volatile  
637 influx and  $\text{SO}_2$  disproportionation, hence, this explains the lack of correlation between  $\delta^{34}\text{S}$  values and Te,

638 Se, Co and As at the mineral-scale at Mala (Fig. 12). To investigate this process, further high-resolution *in*  
639 *situ* isotopic and trace element geochemistry and information on the diffusion rates of trace metals and  
640 sulfur in pyrite (e.g., Cherniak 2010) is needed to understand chemical zonation at the scale of individual  
641 mineral grains.

## 642 Summary and conclusion

643 The distribution of trace metals between different pyrite textures in the Mala VMS deposit appears broadly  
644 analogous to actively forming mafic SMS deposits. Colloform pyrite that formed near the seawater interface  
645 is enriched in low temperature elements such as As and Au relative to massive samples that contain euhedral  
646 pyrite that are relatively enriched in high temperature metals Se, Co and Te. Granular samples that formed  
647 during the reworking of massive pyrite are depleted in all metals (except Te) due to the mobilization and  
648 leaching of metals during low temperature fluid flow at the margin of the VMS mound. There is no  
649 systematic variation in trace metal enrichment profiles with depth in the VMS mound, instead variation  
650 between individual samples can be attributed to dynamic fluid flow patterns within the VMS mound and  
651 the localised (cm to m scale) zone refining of metals around individual fluid conduits that vary spatially  
652 and temporally during mound growth (Fig. 12). All pyrite textures appear to be enriched in Se relative to  
653 both Troodos VMS deposits and mafic hosted VMS deposits more widely indicating a Se-rich magmatic  
654 volatile dominated source.

655 The large range in the  $\delta^{34}\text{S}$  composition of pyrite relative to previous studies and mafic VMS deposits more  
656 widely can be explained by varying combinations of four main processes: i) TSR, ii) leaching of  
657 sulfur/sulfide from host rocks, iii)  $\text{SO}_2$  disproportionation and iv) BSR. Thermochemical sulfate reduction  
658 of seawater and the leaching of igneous sulfur/sulfide generates  $\delta^{34}\text{S}$  values in pyrite that are higher than  
659 the Troodos magmatic mean of 0-1‰, whilst low values that are less than this are produced during the  
660 addition of sulfur from the disproportionation of  $\text{SO}_2$  during the degassing of shallow magma chambers.

661 When combined with trace element geochemistry, we suggest low  $\delta^{34}\text{S}$  values (to -17.1‰) formed during  
662 the BSR of seawater in the upper VMS mound at temperatures of <120°C.

663 Mineral-scale sulfur isotope data exhibits notably more variation than the same samples analysed via bulk  
664 rock analytical methods. We observe greater amounts of variation over a single pyrite grain than recorded  
665 across all bulk rock analyses with  $\delta^{34}\text{S}$  values ranging from -10.9 to 2.5‰. Analytical transects across  
666 individual mineral grains indicate that the source of sulfur in the Mala VMS deposit was variable and  
667 alternated between disproportionation of  $\text{SO}_2$ , TSR and the leaching of igneous sulfur/sulfide as the pyrite  
668 grain grew. Such variation is not evident when using bulk analytical techniques for sulfur isotopes and  
669 warrants further detailed investigation.

670 Linking variations in trace metal enrichment profiles and sulfur isotopes is key in understanding the role of  
671 magmatic volatiles as a potential metal source in mafic VMS deposits. However, findings of this study  
672 indicate no simple correlation between magmatic volatile elements such as Te and Se and  $\delta^{34}\text{S}$  values. We  
673 attribute this decoupled relationship to local scale fluid flow within the mound that leads to the  
674 remobilization of trace metals during zone refining. Pyrite retains  $\delta^{34}\text{S}$  values that indicate  
675 disproportionation (<0‰) but can be depleted in magmatic volatile metals.

## 676 [Acknowledgements](#)

677 The authors acknowledge the support of the Geological Survey Department of Cyprus, especially Costas  
678 Costantinou and Andreas Zissimos. We thank Michael Green and Ifigenia Gavriel for discussion and  
679 assistance in the field. This research was partly funded by the NERC SoS consortium grant  
680 NE/M010848/1 “TeaSe: tellurium and selenium cycling and supply” awarded to Cardiff University and by  
681 the Canadian Research Chair program awarded to John W. Jamieson. We thank Stefanie Brueckner and  
682 associate editor Mostafa Fayek for their constructive reviews and editor-in-chief Georges Beaudoin for the  
683 editorial handling of this manuscript.



## 684 References

- 685 Adamides NG (2010) Mafic-dominated volcanogenic sulphide deposits in the Troodos ophiolite, Cyprus  
686 Part 2 – A review of genetic models and guides for exploration. *Appl Earth Sci* 119:193–204
- 687 Alt JC (1994) A sulfur isotopic profile through the Troodos ophiolite, Cyprus: Primary composition and  
688 the effects of seawater hydrothermal alteration. *Geochim Cosmochim Acta* 58:1825–1840
- 689 Alt JC, Shanks WC (2011) Microbial sulfate reduction and the sulfur budget for a complete section of  
690 altered oceanic basalts, IODP Hole 1256D (eastern Pacific). *Earth Planet Sci Lett* 310:73–83
- 691 Andersen C, Theissen-Krah S, Hannington M, Rüpke L, Petersen S (2017) Faulting and off-axis  
692 submarine massive sulfide accumulation at slow spreading mid-ocean ridges: A numerical  
693 modeling perspective. *Geochem Geophys Geosystems* 18:2305–2320
- 694 Banerjee NR, Gillis KM, Muehlenbachs K (2000) Discovery of epidiosites in a modern oceanic setting,  
695 the Tonga forearc. *Geology* 28:151–154
- 696 Barrie CD, Boyce AJ, Boyle AP, Williams PJ, Blake K, Ogawara T, Akai J, Prior DJ (2009) Growth  
697 controls in colloform pyrite. *Am Mineral.* 94:415–42
- 698 Berkenbosch HA, de Ronde CEJ, Gemmell JB, McNeill AW, Goemann K (2012) Mineralogy and  
699 Formation of Black Smoker Chimneys from Brothers Submarine Volcano, Kermadec Arc. *Econ*  
700 *Geol* 107:1613–1633
- 701 Brazilian Metals Group (2013) High-Grade Copper-Zinc Sulphide Mineralisation Identified At Mala  
702 Prospect – Vrechia. [www.bmgil.com.au/investors/annual-reports](http://www.bmgil.com.au/investors/annual-reports). Accessed 30 July 2018
- 703 Brueckner SM, Piercey SJ, Layne GD, Piercey G, Sylvester PJ, (2015) Variations of sulphur isotope  
704 signatures in sulphides from the metamorphosed Ming Cu(–Au) volcanogenic massive sulphide  
705 deposit, Newfoundland Appalachians, Canada. *Miner Deposita* 50:619–640
- 706 Butler IB, Nesbitt RW (1999) Trace element distributions in the chalcopyrite wall of a black smoker  
707 chimney: insights from laser ablation inductively coupled plasma mass spectrometry (LA–ICP–  
708 MS). *Earth Planet Sci Lett* 167:335–345

709 Butterfield DA, Massoth GJ (1994) Geochemistry of north Cleft segment vent fluids: Temporal changes  
710 in chlorinity and their possible relation to recent volcanism. *J Geophys Res Solid Earth* 99:4951–  
711 4968

712 Butterfield DA, McDuff RE, Mottl MJ, Lilley MD, Lupton JE, Massoth GJ (1994) Gradients in the  
713 composition of hydrothermal fluids from the Endeavour segment vent field: Phase separation and  
714 brine loss. *J Geophys Res Solid Earth* 99:9561–9583

715 Butterfield DA, Nakamura K, Takano B, Lilley MD, Lupton JE, Resing JA, Roe KK (2011) High SO<sub>2</sub>  
716 flux, sulfur accumulation, and gas fractionation at an erupting submarine volcano. *Geology* 39:  
717 803–806

718 Cherniak, DJ (2010) Diffusion in Carbonates, Fluorite, Sulfide Minerals, and Diamond. *Rev Mineral*  
719 *Geochem* 72:871–897

720 Cook NJ, Ciobanu CL, Mao J (2009) Textural control on gold distribution in As-free pyrite from the  
721 Dongping, Huangtuliang and Hougou gold deposits, North China Craton (Hebei Province,  
722 China). *Chem Geol* 264:101–121

723 de Ronde CEJ, Massoth GJ, Butterfield DA, Christenson BW, Ishibashi J, Ditchburn RG, Hannington  
724 MD, Brathwaite RL, Lupton JE, Kamenetsky VS, Graham IJ, Zellmer GF, Dziak RP, Embley  
725 RW, Dekov VM, Munnik F, Lahr J, Evans LJ, Takai K, (2011) Submarine hydrothermal activity  
726 and gold-rich mineralization at Brothers Volcano, Kermadec Arc, New Zealand. *Miner Deposita*  
727 46:541–584

728 de Ronde CEJ, Hannington MD, Stoffers P, Wright IC, Ditchburn RG, Reyes AG, Baker ET, Massoth  
729 GJ, Lupton JE, Walker SL, Greene RR, Soong CWR, Ishibashi J, Lebon GT, Bray CJ, Resing JA,  
730 (2005) Evolution of a Submarine Magmatic-Hydrothermal System: Brothers Volcano, Southern  
731 Kermadec Arc, New Zealand. *Econ Geol* 100:1097–1133

732 Edmond JM, Campbell AC, Palmer MR, Klinkhammer GP, German CR, Edmonds HN, Elderfield H,  
733 Thompson G, Rona P (1995) Time series studies of vent fluids from the TAG and MARK sites

734 (1986, 1990) Mid-Atlantic Ridge: a new solution chemistry model and a mechanism for Cu/Zn  
735 zonation in massive sulphide orebodies. *Geol Soc Lond Spec Publ* 87:77–86

736 Eldridge CW, Barton PB, and Ohmoto H (1983) Mineral textures and their bearing on formation of the  
737 Kuroko orebodies. *Econ Geol Mono* 5: 241–281

738 Fallon EK, Petersen S, Brooker RA, Scott TB (2017) Oxidative dissolution of hydrothermal mixed-  
739 sulphide ore: An assessment of current knowledge in relation to seafloor massive sulphide  
740 mining. *Ore Geol Rev* 86:309–337

741 Farquhar J, Johnston DT, Wing BA, Habicht KS, Canfield DE, Airieau S, Thiemens MH (2003) Multiple  
742 sulphur isotopic interpretations of biosynthetic pathways: implications for biological signatures in  
743 the sulphur isotope record. *Geobiology* 1:27–36

744 Fox S, Katzir Y, Bach W, Schlicht L, Glessner J (2020) Magmatic volatiles episodically flush oceanic  
745 hydrothermal systems as recorded by zoned epidote. *Commun Earth Environ* 1:52

746 Fuchs S, Hannington MD, Petersen S (2019) Divining gold in seafloor polymetallic massive sulfide  
747 systems. *Miner Deposita* 54:789–820

748 Galley AG, Hannington MD, Jonasson IR (2007). Volcanogenic massive sulphide deposits, in: *Mineral*  
749 *Deposits of Canada: A Synthesis of Major Deposit Types*. Geological Association of Canada, St.  
750 John's, Newfoundland, pp.141–162

751 Gass IG (1968) Is the Troodos Massif of Cyprus a Fragment of Mesozoic Ocean Floor? *Nature* 220:39–  
752 42

753 Gass IG, Smewing JD, (1973) Intrusion, Extrusion and Metamorphism at Constructive Margins: Evidence  
754 from the Troodos Massif, Cyprus. *Nature* 242:26–29

755 Gemmel JB, Sharpe R, Jonasson IR, Herzig PM (2004) Sulfur Isotope Evidence for Magmatic  
756 Contributions to Submarine and Subaerial Gold Mineralization: Conical Seamount and the  
757 Ladolam Gold Deposit, Papua New Guinea. *Econ Geol* 99:1711–1725

758 Genna D, Gaboury D (2015) Deciphering the Hydrothermal Evolution of a VMS System by LA-ICP-MS  
759 Using Trace Elements in Pyrite: An Example from the Bracemac-McLeod Deposits, Abitibi,  
760 Canada, and Implications for Exploration. *Econ Geol* 110:2087–2108

761 Gillis KM, Roberts MD (1999) Cracking at the magma–hydrothermal transition: evidence from the  
762 Troodos Ophiolite, Cyprus. *Earth Planet Sci Lett* 169:227–244

763 Grant HLJ, Hannington MD, Petersen S, Frische M, Fuchs SH (2018) Constraints on the behavior of trace  
764 elements in the actively-forming TAG deposit, Mid-Atlantic Ridge, based on LA-ICP-MS  
765 analyses of pyrite. *Chem Geol* 498:45–71

766 Habicht KS, Canfield DE (1997) Sulfur isotope fractionation during bacterial sulfate reduction in organic-  
767 rich sediments. *Geochim Cosmochim Acta* 61:5351–5361

768 Halbach P, Blum N, Münch U, Plüger W, Garbe-Schönberg D, Zimmer M (1998) Formation and decay of  
769 a modern massive sulfide deposit in the Indian Ocean. *Miner Deposita* 33:302–309

770 Hannington MD, Bleeker W, Kjarsgaard I (1999) Sulfide Mineralogy, Geochemistry, and Ore Genesis of  
771 the Kidd Creek Deposit: Part II. The Bornite Zone\*, in: Hannington, MD, Barrie CT (ed), *The*  
772 *Giant Kidd Creek Volcanogenic Massive Sulfide Deposit, Western Abitibi Subprovince, Canada.*  
773 *Society of Economic Geologists, Littleton Colorado*

774 Hannington MD, de Ronde CEJ, Petersen S (2005) Sea-floor tectonics and submarine hydrothermal  
775 systems, in: Hedenquist JW, Thompson JFH, Goldfarb RJ, Richards JP (ed.), *Economic Geology*  
776 *100th Anniversary Volume.* Society of Economic Geologists, Littleton, Colorado, USA, pp. 111–  
777 141

778 Hannington MD, Galley AG, Herzig PM, Petersen S (1998) Comparison of the TAG mound and  
779 stockwork complex with Cyprus-type massive sulfide deposits. In: Herzig, P.M., Humphris, S.E.,  
780 Miller, D.J., and Zierenberg, R.A. (ed), 1998 *Proceedings of the Ocean Drilling Program,*  
781 *Scientific Results, Vol. 158*

782 Herzig PM, Hannington MD, Arribas Jr. A (1998) Sulfur isotopic composition of hydrothermal  
783 precipitates from the Lau back-arc: implications for magmatic contributions to seafloor  
784 hydrothermal systems. *Miner Deposita* 33:226–237

785 Herzig PM, Hannington MD, Scott SD, Maliotis G, Rona PA, Thompson G (1991) Gold-rich sea-floor  
786 gossans in the Troodos Ophiolite and on the Mid-Atlantic Ridge. *Econ Geol* 86:1747–1755

787 Humphris SE, Herzig PM, Miller DJ, Alt JC, Becker K, Brown D, Brüggmann G, Chiba H, Fouquet Y,  
788 Gemmell JB, Guerin G, Hannington MD, Holm NG, Honnorez JJ, Iturrino GJ, Knott R, Ludwig  
789 R, Nakamura K, Petersen S, Reysenbach A-L, Rona PA, Smith S, Sturz AA, Tivey MK, Zhao X,  
790 (1995) The internal structure of an active sea-floor massive sulphide deposit. *Nature* 377:713–716

791 Huston DL, Relvas JMRS, Gemmell JB, Drieberg S (2011) The role of granites in volcanic-hosted  
792 massive sulphide ore-forming systems: an assessment of magmatic–hydrothermal contributions.  
793 *Miner Deposita* 46:473–507

794 Huston DL, Sie SH, Suter GF (1995) Selenium and its importance to the study of ore genesis: the  
795 theoretical basis and its application to volcanic-hosted massive sulfide deposits using pixeprobe  
796 analysis. *Nucl. Instrum. Methods Phys Res Sect B Beam Interact Mater At, Nuclear Microprobe  
797 Technology and Applications* 104:476–480

798 Jamieson JW, Hannington MD, Clague DA, Kelley DS, Delaney JR, Holden JF, Tivey MK, Kimpe LE,  
799 (2013) Sulfide geochronology along the Endeavour Segment of the Juan de Fuca Ridge.  
800 *Geochem Geophys Geosystems* 14:2084–2099

801 Jowitt SM, Jenkin GRT, Coogan LA, Naden J (2012). Quantifying the release of base metals from source  
802 rocks for volcanogenic massive sulfide deposits: Effects of protolith composition and alteration  
803 mineralogy. *J Geochem Explor* 118:47–59

804 Kampschulte A, Strauss H (2004) The sulfur isotopic evolution of Phanerozoic seawater based on the  
805 analysis of structurally substituted sulfate in carbonates. *Chem Geol* 204:255–286

806 Keith M, Haase KM, Klemm R, Krumm S, Strauss H (2016a) Systematic variations of trace element and  
807 sulfur isotope compositions in pyrite with stratigraphic depth in the Skouriotissa volcanic-hosted  
808 massive sulfide deposit, Troodos ophiolite, Cyprus. *Chem Geol* 423:7–18

809 Keith M, Haase KM, Klemm R, Smith DJ, Schwarz-Schampera U, Bach W (2018) Constraints on the  
810 source of Cu in a submarine magmatic-hydrothermal system, Brothers volcano, Kermadec island  
811 arc. *Contrib Mineral Petrol* 173:40

812 Keith M, Häckel F, Haase KM, Schwarz-Schampera U, Klemm R, (2016b) Trace element systematics of  
813 pyrite from submarine hydrothermal vents. *Ore Geol Rev* 72:728–745

814 Kim J, Lee I, Lee K-Y (2004) S, Sr, and Pb isotopic systematics of hydrothermal chimney precipitates  
815 from the Eastern Manus Basin, western Pacific: Evaluation of magmatic contribution to  
816 hydrothermal system. *J Geophys Res Solid Earth* 109

817 Kleinrock MC, Humphris SE (1996) Structural control on sea-floor hydrothermal activity at the TAG  
818 active mound. *Nature* 382:149–153

819 Kusakabe M, Komoda Y, Takano B, Abiko T (2000) Sulfur isotopic effects in the disproportionation  
820 reaction of sulfur dioxide in hydrothermal fluids: implications for the  $\delta^{34}\text{S}$  variations of dissolved  
821 bisulfate and elemental sulfur from active crater lakes. *J Volcanol Geotherm Res* 97:287–307

822 LaFlamme C, Barré G, Fiorentini ML, Beaudoin G, Occhipinti S, Bell J (2021) A significant seawater  
823 sulfate reservoir at 2.0 Ga determined from multiple sulfur isotope analyses of the  
824 Paleoproterozoic Degruusa Cu-Au volcanogenic massive sulfide deposit, Western Australia.  
825 *Geochim Cosmochim Acta* 295:178–193

826 Lalou C, Münch U, Halbach P, Reyss J-L (1998) Radiochronological investigation of hydrothermal  
827 deposits from the MESO zone, Central Indian Ridge. *Mar Geol* 149:243–254

828 Lalou C, Reyss J-L, Brichet E, Arnold M, Thompson G, Fouquet Y, Rona PA (1993) New age data for  
829 Mid-Atlantic Ridge hydrothermal sites: TAG and Snakepit chronology revisited. *J Geophys Res*  
830 98:9705–9713

831 Lalou C, Thompson G, Arnold M, Brichet E, Druffel E, Rona PA (1990) Geochronology of TAG and  
832 Snakepit hydrothermal fields, Mid-Atlantic Ridge: witness to a long, complex hydrothermal  
833 history. *Earth Planet Sci Lett* 97:113-128

834 Layton-Matthews D, Leybourne MI, Peter JM, Scott SD, Cousens B, Eglington BM (2013) Multiple  
835 sources of selenium in ancient seafloor hydrothermal systems: Compositional and Se, S, and Pb  
836 isotopic evidence from volcanic-hosted and volcanic-sediment-hosted massive sulfide deposits of  
837 the Finlayson Lake District, Yukon, Canada. *Geochim Cosmochim Acta* 117:313–331

838 Layton-Matthews D, Peter JM, Scott SD, Leybourne MI (2008) Distribution, Mineralogy, and  
839 Geochemistry of Selenium in Felsic Volcanic-Hosted Massive Sulfide Deposits of the Finlayson  
840 Lake District, Yukon Territory, Canada. *Econ Geol* 103:61–88

841 Lode S, Piercey SJ, Layne GD, Piercey G, Cloutier J (2017) Multiple sulphur and lead sources recorded  
842 in hydrothermal exhalites associated with the Lemarchant volcanogenic massive sulphide deposit,  
843 central Newfoundland, Canada. *Miner Deposita* 52:105-128

844 Lüders V, Pracejus B, Halbach P (2001) Fluid inclusion and sulfur isotope studies in probable modern  
845 analogue Kuroko-type ores from the JADE hydrothermal field (Central Okinawa Trough, Japan).  
846 *Chem Geol* 173:45–58

847 Martin AJ, Keith M, McDonald I, Haase KM, McFall KA, Klemd R, MacLeod CJ (2019) Trace element  
848 systematics and ore-forming processes in mafic VMS deposits: Evidence from the Troodos  
849 ophiolite, Cyprus. *Ore Geol Rev* 106:205–225

850 Martin AJ, Keith M, Parvaz DB, McDonald I, Boyce AJ, McFall KA, Jenkin GRT, Strauss H, MacLeod  
851 CJ (2020) Effects of magmatic volatile influx in mafic VMS hydrothermal systems: Evidence  
852 from the Troodos ophiolite, Cyprus. *Chem Geol* 531:119325

853 Martin AJ, McDonald I, MacLeod CJ, Prichard HM, McFall K (2018) Extreme enrichment of selenium in  
854 the Apliki Cyprus-type VMS deposit, Troodos, Cyprus. *Min Mag* 82:697–724

855 Martin AJ, McDonald I, Jenkin GRT, McFall KA, Boyce AJ, Jamieson JW, MacLeod CJ (2021) A  
856 missing link between ancient and active mafic-hosted seafloor hydrothermal systems –  
857 Magmatic volatile influx in the exceptionally preserved Mala VMS deposit, Troodos, Cyprus.  
858 Chem Geol 567:120127

859 Maslennikov VV, Maslennikova SP, Large RR, Danyushevsky LV (2009) Study of Trace Element  
860 Zonation in Vent Chimneys from the Silurian Yaman-Kasy Volcanic-Hosted Massive Sulfide  
861 Deposit (Southern Urals, Russia) Using Laser Ablation-Inductively Coupled Plasma Mass  
862 Spectrometry (LA-ICPMS). Econ Geol 104:1111–1141

863 Mathieu L (2019) Detecting magmatic-derived fluids using pyrite chemistry: Example of the  
864 Chibougamau area, Abitibi Subprovince, Québec. Ore Geol Rev 114:103-127

865 McDermott JM, Ono S, Tivey MK, Seewald JS, Shanks WC, Solow AR (2015) Identification of sulfur  
866 sources and isotopic equilibria in submarine hot-springs using multiple sulfur isotopes. Geochim  
867 Cosmochim Acta 160:169–187

868 McDonald MJ, Piercey SJ, Layne GD, Pigage LC, Piercey G (2018) Mineral Assemblages, Textures and  
869 In Situ Sulphur Isotope Geochemistry of Sulphide Mineralization from the Cyprus-Type Ice  
870 Volcanogenic Massive Sulphide (VMS) Deposit, Yukon, Canada. Minerals 8:501

871 McPhail DC (1995) Thermodynamic properties of aqueous tellurium species between 25 and 350°.  
872 Geochim Cosmochim Acta 59:851–866

873 Melekestseva IY, Tret'yakov GA, Nimis P, Yuminov AM, Maslennikov VV, Maslennikova SP,  
874 Kotlyarov VA, Beltenev VE, Danyushevsky LV, Large R (2014) Barite-rich massive sulfides  
875 from the Semenov-1 hydrothermal field (Mid-Atlantic Ridge, 13°30.87' N): Evidence for phase  
876 separation and magmatic input. Mar Geol 349:37–54

877 Meng X, Li X, Chu F, Fu B, Lei J, Li Z, Wang H, Chen L (2019) Multi-stage growth and fluid  
878 evolution of a hydrothermal sulphide chimney in the East Pacific Ridge 1–2° S hydrothermal  
879 field: constraints from in situ sulphur isotopes. Geol Mag 156:989–1002



880 Meng X, Li X, Chu F, Zhu J, Lei J, Li Z, Wang H, Chen L, Zhu Z (2020) Trace element and sulfur  
881 isotope compositions for pyrite across the mineralization zones of a sulfide chimney from the  
882 East Pacific Rise (1-2°S). *Ore Geol Rev* 116:103209

883 Monecke T, Petersen S, Hannington MD, Grant H, Samson I (2016) The minor element endowment  
884 of modern sea-floor massive sulfides and comparison with deposits hosted in ancient  
885 volcanic successions. *Rev Econ Geol* 18:245-306

886 Muenow DW, Garciat MO, Aggrey KE, Bednarz U, Schmincke HU (1990) Volatiles in submarine  
887 glasses as a discriminant of tectonic origin: application to the Troodos ophiolite. *Nature* 343:  
888 159–161

889 Mukasa SB, Ludden JN (1987) Uranium-lead isotopic ages of plagiogranites from the Troodos ophiolite,  
890 Cyprus, and their tectonic significance. *Geology* 15:825–828

891 Murton BJ, Lehrmann B, Dutrieux AM, Martins S, de la Iglesia AG, Stobbs IJ, Barriga FJAS, Bialas J,  
892 Dannowski A, Vardy ME, North LJ, Yeo IALM, Lusty PAJ, Petersen S (2019) Geological fate of  
893 seafloor massive sulphides at the TAG hydrothermal field (Mid-Atlantic Ridge). *Ore Geol Rev*  
894 107:903–925

895 Ohmoto H (1996) Formation of volcanogenic massive sulfide deposits: The Kuroko perspective. *Ore*  
896 *Geol Rev* 10:135–177

897 Ohmoto H, Lasaga AC (1982) Kinetics of reactions between aqueous sulfates and sulfides in  
898 hydrothermal systems. *Geochim Cosmochim Acta* 46:1727–1745

899 Ono S, Shanks WC, Rouxel OJ, Rumble D (2007) S-33 constraints on the seawater sulfate contribution in  
900 modern seafloor hydrothermal vent sulfides. *Geochim Cosmochim Acta* 71:1170–1182

901 Parvaz DB, 2014. Oxidation Zones of Volcanogenic Massive Sulphide Deposits in the Troodos Ophiolite,  
902 Cyprus: Targeting Secondary Copper Deposits. Doctoral Thesis, University of Exeter

903 Patten CGC, Pitcairn IK, Alt JC, Zack T, Lahaye Y, Teagle DAH, Markdahl, K., 2020. Metal fluxes  
904 during magmatic degassing in the oceanic crust: sulfide mineralisation at ODP site 786B, Izu-  
905 Bonin forearc. *Miner Deposita* 55, 469–489

906 Patten CGC, Pitcairn IK, Teagle DAH, (2017) Hydrothermal mobilisation of Au and other metals in  
907 supra-subduction oceanic crust: Insights from the Troodos ophiolite. *Ore Geol Rev* 86:487–508

908 Pearce JA, Robinson PT (2010) The Troodos ophiolitic complex probably formed in a subduction  
909 initiation, slab edge setting. *Gondwana Res, A Tribute to Miyashiro* 18:60–81

910 Pedersen L-ER, Staudigel H, McLoughlin N, Whitehouse MJ, Strauss H (2017) A multiple sulfur isotope  
911 study through the volcanic section of the Troodos ophiolite. *Chem Geol* 46:849–62

912 Petersen S, Herzig PM, Hannington MD (2000) Third dimension of a presently forming VMS deposit:  
913 TAG hydrothermal mound, Mid-Atlantic Ridge, 26°N. *Miner Deposita* 35:233–259

914 Petersen S, Herzig PM, Hannington MD, Jonasson IR, Arribas A (2002) Submarine Gold Mineralization  
915 Near Lihir Island, New Ireland Fore-Arc, Papua New Guinea. *Econ Geol* 97:1795–1813

916 Prichard HM, Knight RD, Fisher PC, McDonald I, Zhou M-F, Wang CY (2013) Distribution of platinum-  
917 group elements in magmatic and altered ores in the Jinchuan intrusion, China: an example of  
918 selenium remobilization by postmagmatic fluids. *Miner Deposita* 48:767–786

919 Rautenschlein M, Jenner GA, Hertogen J, Hofmann AW, Kerrich R, Schmincke H-U, White WM (1985)  
920 Isotopic and trace element composition of volcanic glasses from the Akaki Canyon, Cyprus:  
921 implications for the origin of the Troodos ophiolite. *Earth Planet Sci Lett* 75:369–383

922 Reed MH, Palandri J (2006) Sulfide Mineral Precipitation from Hydrothermal Fluids. *Rev Mineral*  
923 *Geochem* 61:609–631

924 Revan MK, Genç Y, Maslennikov VV, Maslennikova SP, Large RR, Danyushevsky LV (2014)  
925 Mineralogy and trace-element geochemistry of sulfide minerals in hydrothermal chimneys from  
926 the Upper-Cretaceous VMS deposits of the eastern Pontide orogenic belt (NE Turkey). *Ore Geol*  
927 *Rev* 63:129–149

928 Richardson CJ, Cann JR, Richards HG, Cowan JG (1987) Metal-depleted root zones of the Troodos ore-  
929 forming hydrothermal systems, Cyprus. *Earth Planet Sci Lett* 84:243–253

930 Rouxel O, Fouquet Y, Ludden JN (2004) Subsurface processes at the lucky strike hydrothermal field,  
931 Mid-Atlantic ridge: evidence from sulfur, selenium, and iron isotopes. *Geochim Cosmochim Acta*  
932 68:2295–2311

933 Rouxel O, Ono S, Alt J, Rumble D, Ludden J (2008) Sulfur isotope evidence for microbial sulfate  
934 reduction in altered oceanic basalts at ODP Site 801. *Earth Planet Sci Lett* 268:110–123

935 Sakai H (1968) Isotopic properties of sulfur compounds in hydrothermal processes. *Geochem J* 2:29–49

936 Shanks WC (2001) Stable Isotopes in Seafloor Hydrothermal Systems: Vent fluids, hydrothermal  
937 deposits, hydrothermal alteration, and microbial processes. *Rev Mineral Geochem* 43:469–525

938 Sharman ER, Taylor BE, Minarik WG, Dubé B, Wing BA (2015) Sulfur isotope and trace element data  
939 from ore sulfides in the Noranda district (Abitibi, Canada): implications for volcanogenic massive  
940 sulfide deposit genesis. *Miner Deposita* 50:591–606

941 Sillitoe RH, Hannington MD, Thompson JFH (1996) High sulfidation deposits in the volcanogenic  
942 massive sulfide environment. *Econ Geol* 91:204–212

943 Tivey MK (2007) Generation of Seafloor Hydrothermal Vent Fluids and Associated Mineral Deposits.  
944 *Oceanography* 20:50–65

945 Tivey MK, Humphris SE, Thompson G, Hannington MD, Rona PA (1995). Deducing patterns of fluid  
946 flow and mixing within the TAG active hydrothermal mound using mineralogical and  
947 geochemical data. *J Geophys Res Solid Earth* 100:12527–12555.

948 Varga RJ, Moores EM (1985) Spreading structure of the Troodos ophiolite, Cyprus. *Geology* 13:846–  
949 850.

950 Von Damm KL, Oosting SE, Kozlowski R, Buttermore LG, Colodner DC, Edmonds HN, Edmond JM,  
951 Grebmeier JM (1995) Evolution of East Pacific Rise hydrothermal vent fluids following a  
952 volcanic eruption. *Nature* 375:47–50

953 Von Damm KL (1995) Controls on the Chemistry and Temporal Variability of Seafloor Hydrothermal  
954 Fluids. In: SE Humphris, Zierenberg RA, Mullineaux LS, Thomson RE (ed) *Seafloor*

955 Hydrothermal Systems: Physical, Chemical, Biological, and Geological Interactions. American  
956 Geophysical Union, Washington D.C., vol.91 pp. 222–247

957 Wang Y, Han X, Petersen S, Frische M, Qiu Z, Cai Y, Zhou P (2018) Trace Metal Distribution in Sulfide  
958 Minerals from Ultramafic-Hosted Hydrothermal Systems: Examples from the Kairei Vent Field,  
959 Central Indian Ridge. *Minerals* 8:526

960 Woelki D, Regelous M, Haase KM, Romer RHW, Beier C (2018) Petrogenesis of boninitic lavas from  
961 the Troodos Ophiolite, and comparison with Izu–Bonin–Mariana fore-arc crust. *Earth Planet Sci*  
962 *Lett.* 498:203–214

963 Wohlgemuth-Ueberwasser CC, Viljoen F, Petersen S, Vorster C (2015) Distribution and solubility limits  
964 of trace elements in hydrothermal black smoker sulfides: An in-situ LA-ICP-MS study. *Geochim*  
965 *Cosmochim Acta* 159:16–41

966 Woodruff LG, Shanks WC (1988) Sulfur isotope study of chimney minerals and vent fluids from 21°N,  
967 East Pacific Rise: Hydrothermal sulfur sources and disequilibrium sulfate reduction. *J Geophys*  
968 *Res Solid Earth* 93:4562–4572

969 Wortmann UG, Bernasconi SM, Böttcher ME (2001) Hypersulfidic deep biosphere indicates extreme  
970 sulfur isotope fractionation during single-step microbial sulfate reduction. *Geology* 29:647–650

971 Yamamoto M (1976) Relationship between Se/S and sulfur isotope ratios of hydrothermal sulfide  
972 minerals. *Mineral Deposita* 11:197–209

973 Yang K, Scott SD (2002) Magmatic Degassing of Volatiles and Ore Metals into a Hydrothermal System  
974 on the Modern Sea Floor of the Eastern Manus Back-Arc Basin, Western Pacific. *Econ Geol* 97:  
975 1079–1100

976 Yang K, Scott SD (1996) Possible contribution of a metal-rich magmatic fluid to a sea-floor hydrothermal  
977 system. *Nature* 383:420–423

978 Yeats CJ, Parr JM, Binns RA, Gemmill JB, Scott SD (2014) The SuSu Knolls Hydrothermal Field,  
979 Eastern Manus Basin, Papua New Guinea: An Active Submarine High-Sulfidation Copper-Gold  
980 System. *Econ Geol* 109:2207–2226

981 You C-F, Bickle MJ (1998) Evolution of an active sea-floor massive sulphide deposit. *Nature* 394:668–  
982 671  
983 Zeng Z, Ma Y, Chen S, Selby D, Wang X, Yin X (2017) Sulfur and lead isotopic compositions of  
984 massive sulfides from deep-sea hydrothermal systems: Implications for ore genesis and fluid  
985 circulation. *Ore Geol Rev* 87:155–171

## 986 Figure Captions

987 Figure 1: Simplified geological map of the Troodos ophiolite, Cyprus. Graben axes are indicated by the  
988 dashed lines. Mala is located in the SW of the ophiolite at the LPL/BG transitional horizon (after Martin et  
989 al. 2018).

990 Figure 2: Field observations from the Mala VMS deposit. A) The exposed portion of the Mala mound. The  
991 VMS mound contains pyrite and crudely layered gypsum capped by a veneer of leached volcanic rocks.  
992 The margin of the VMS mound is denoted by the white dashed line. B) Coarse-grained euhedral pyrite with  
993 infilling gypsum (white). C) Massive pyrite. D) Massive gypsum horizon located in the upper mound region  
994 containing coarse (1-2 cm) euhedral pyrite grains. E) Gypsum containing finely disseminated euhedral  
995 pyrite. F) Euhedral pyrite in a gypsum matrix with minor Fe oxide staining. G) Aggregates of euhedral  
996 pyrite in gypsum.

997 Figure 3: Photomicrographs in reflected light of common pyrite textures at Mala. A) Massive pyrite. Note  
998 porous inclusion trails delineating crystal growth zones. B) The relationship between massive and dendritic  
999 pyrite textures. C) Dendritic pyrite. D) Colloform pyrite in a matrix of porous pyrite. E) Granular pyrite  
1000 consisting of anhedral rounded pyrite in a matrix of Fe-oxides and pyrite. F) Finely disseminated euhedral  
1001 to subhedral pyrite in surrounding altered volcanic rocks.

1002 Figure 4: Pyrite chemistry analysed via LA-ICP-MS. Pyrite analyses are divided based on grain morphology  
1003 into disseminated (n=78), massive (n=40), granular (n=10) and colloform (n=15). Analyses that are below  
1004 detection limit are excluded (Table S1, ESM). A) Te vs. Co, B) Te vs. Se, C) Co vs. Se. D) Total measured

1005 trace metal by pyrite texture (Co, Ni, Cu, Zn, As, Se, Ag, Cd, Sb, Te, Re, Au, Pb and Bi). Data in ESM,  
1006 Table S1.

1007 Figure 5: Pyrite chemistry analysed via LA-ICP-MS from the core (n=35) and rim (n=43) of individual  
1008 disseminated pyrite grains. The rim of pyrite grains are enriched in Co and Cu and relative to the margin.  
1009 Data in ESM, Table S1.

1010 Figure 6: Summary of sulfur isotope analyses ( $\delta^{34}\text{S}$ ) analysed by SIMS (n=31) and classified based on pyrite  
1011 texture. Massive pyrite exhibits the largest range in its  $\delta^{34}\text{S}$  composition whilst colloform pyrite clusters  
1012 between 0 and -5‰. Data and standard information in ESM, Table S3.

1013 Figure 7: SIMS spot analyses across disseminated pyrite grains. Lower images are the same grain etched  
1014 with NaOCl to reveal any internal zonations. A) Sample MAL 05 (in the lower image “SG” refers to  
1015 different sub-grains), B) sample MAL 11-A, C) MAL 11-B.

1016 Figure 8: LA-ICP-MS analyses for individual mineral grains. A) Se vs. As, B) Se vs. Te, C) Se vs. Co. Data  
1017 in Table S1 and sample description in Figure S1, ESM.

1018 Figure 9: A comparison between bulk  $\delta^{34}\text{S}$  analyses of Mala samples (Martin et al. 2021) with the same  
1019 sub-set of samples analysed by SIMS in this study. Samples analysed by SIMS exhibit notably more  
1020 variation with extremely low (-17.1‰) and high (7.5‰) values compared to the samples analysed using  
1021 bulk methods. Cretaceous seawater 18 to 19‰ (SW) (Kampschulte and Strauss 2004) and Troodos  
1022 magmatic mean 0 to 1‰ (TO magmatic mean; Alt 1994).

1023 Figure 10: Coupled trace metal and  $\delta^{34}\text{S}$  analyses across individual disseminated pyrite grains. A) Sample  
1024 MAL 05. B) Sample MAL 11 A. C) Sample MAL 11 B. P1 on X axis refers to the specific analytical point  
1025 in the image above. Selenium, As, Co and Te concentrations are shown by red lines with corresponding  
1026 concentration in ppm on the secondary axis (right). Note varying Y axis between graphs.

1027 Figure 11: Se, Te and Co vs.  $\delta^{34}\text{S}$  for all samples. Twinned points in disseminated pyrite (as in Fig. 10) are  
1028 represented by multiple analytical points. In samples where points were not twinned an average value is  
1029 reported and denoted by \* next to each sample in the legend. A) Se vs.  $\delta^{34}\text{S}$ , B) Te vs.  $\delta^{34}\text{S}$ , C) Co vs.  $\delta^{34}\text{S}$ .  
1030 Volatile trend in plot B shows expected trend between Te, Se and Co and  $\delta^{34}\text{S}$ . The grey box represents the  
1031 primary magmatic mean for Troodos magmatic rocks (Alt 1994). Solid line represents the average bulk  
1032  $\delta^{34}\text{S}$  for all Troodos VMS (4.6‰; Martin et al. 2020) and the dashed line is the bulk median  $\delta^{34}\text{S}$  for Mala  
1033 (-4.3‰; Martin et al. 2021).

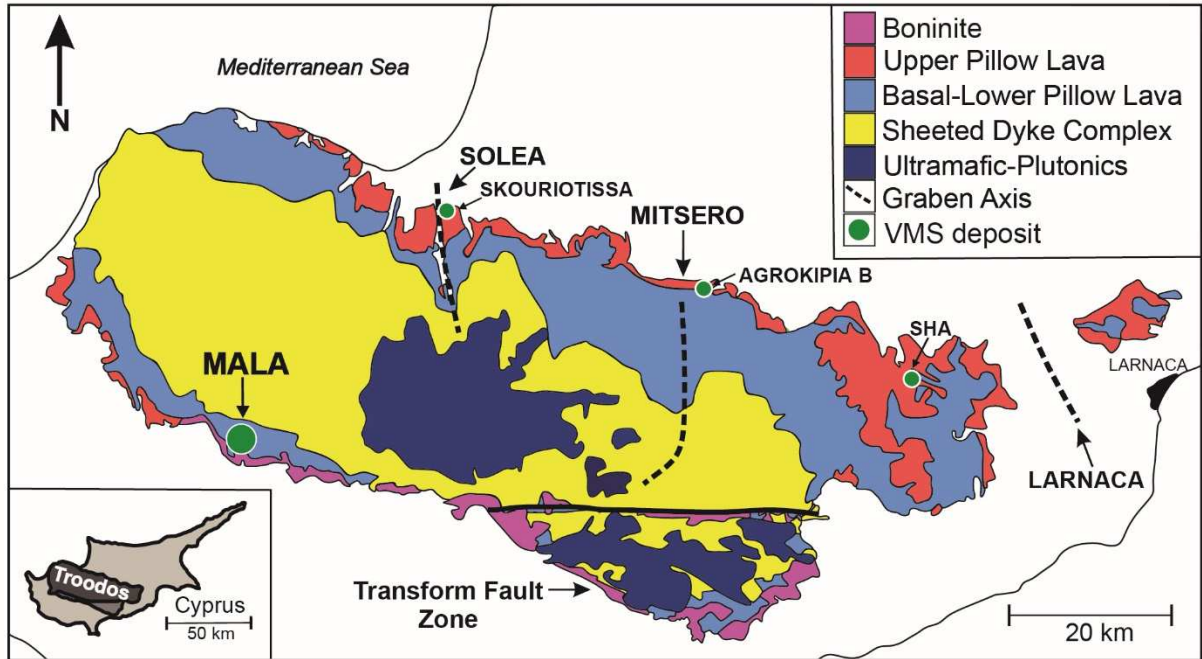
1034 Figure 12: A) Summary schematic for mound scale metal enrichment processes at the Mala VMS deposit.  
1035 Granular pyrite forms from the reworking and collapse of the outer mound and chimney material, metals  
1036 are remobilized during low temperature fluid flow. Disseminated pyrite forms in gypsum veins and volcanic  
1037 rocks (Fig. 2). B) Colloform and dendritic textured pyrite (Fig. 3 C and D) form at the margin of the sulfide  
1038 mound where seawater ingress is high creating disequilibrium textures and fluid temperatures are lower  
1039 (<350°C) leading to an enrichment in Ag, Au and Pb. C) With increasing time, permeability pathways  
1040 within the mound change in response to the collapse and reworking of anhydrite, creating a prominent  
1041 brecciated texture leading to localised zone refining on the cm/m scale in response to new high temperature  
1042 fluid pathways. D) Pyrite grains undergo zone refining leading to the decoupling of  $\delta^{34}\text{S}$  and magmatic  
1043 volatile elements in pyrite.

## 1044 Table Captions

1045 Table 1: Summary of pyrite geochemistry classified by texture: colloform (n=15), granular (n=10),  
1046 massive (n=40) and disseminated (n=78). Points that were below detection limit (Table S1 and S2, ESM)  
1047 are excluded (n > DL = number of analyses above detection limit).

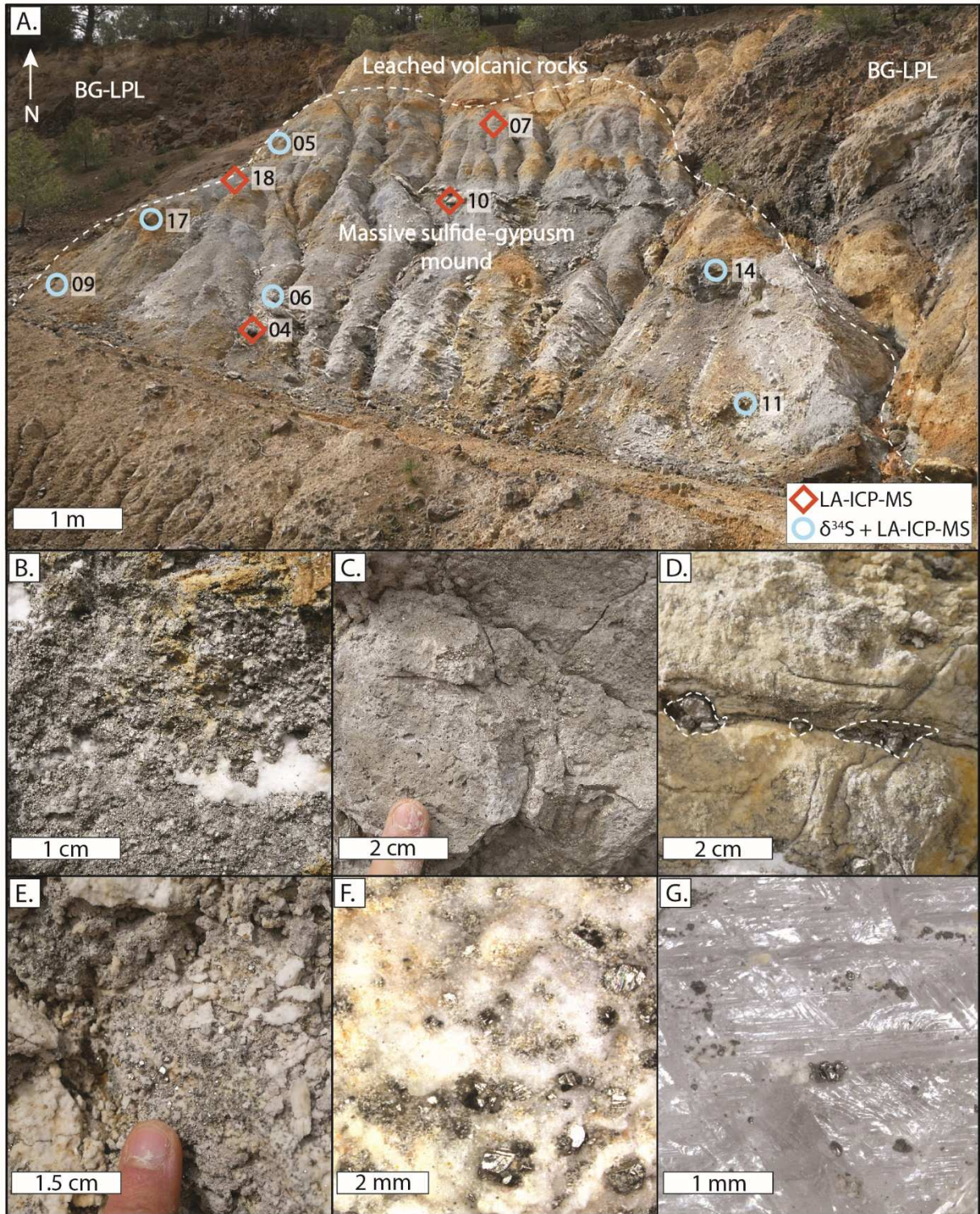
1048

1049



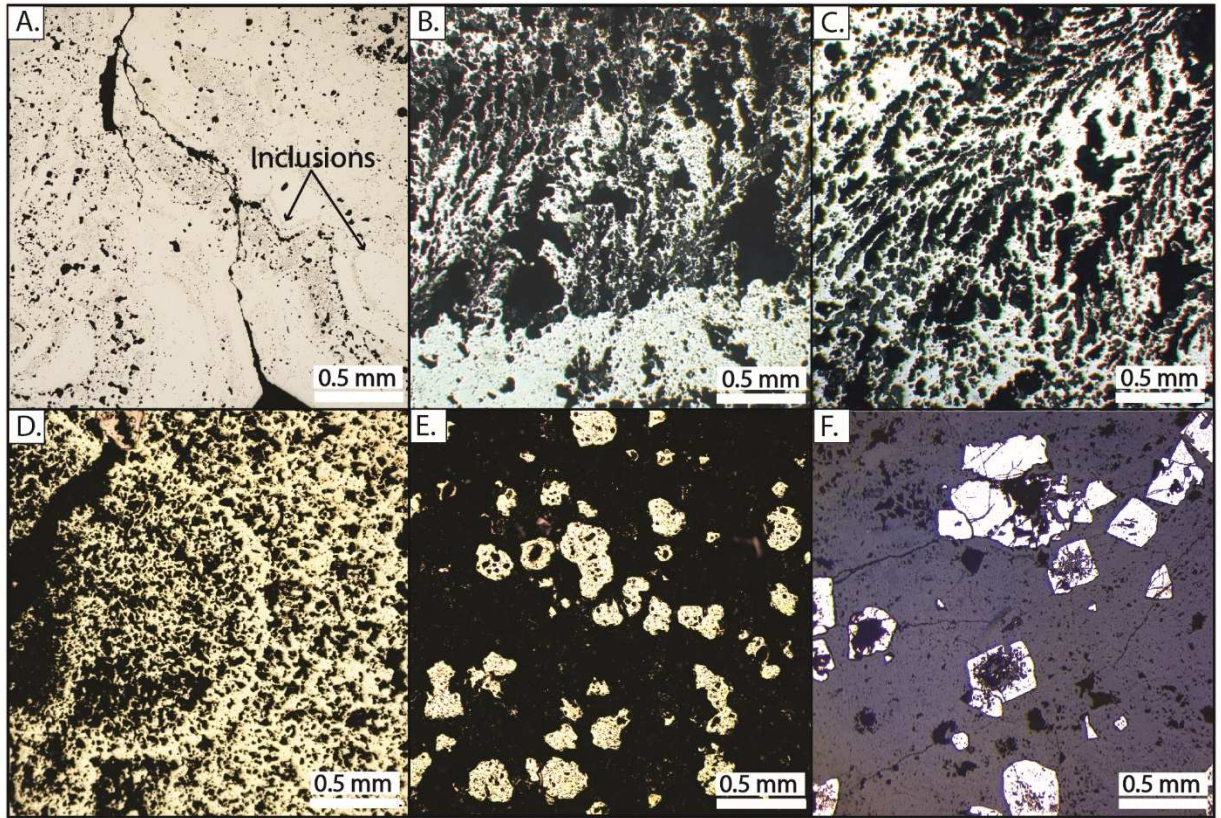
1050



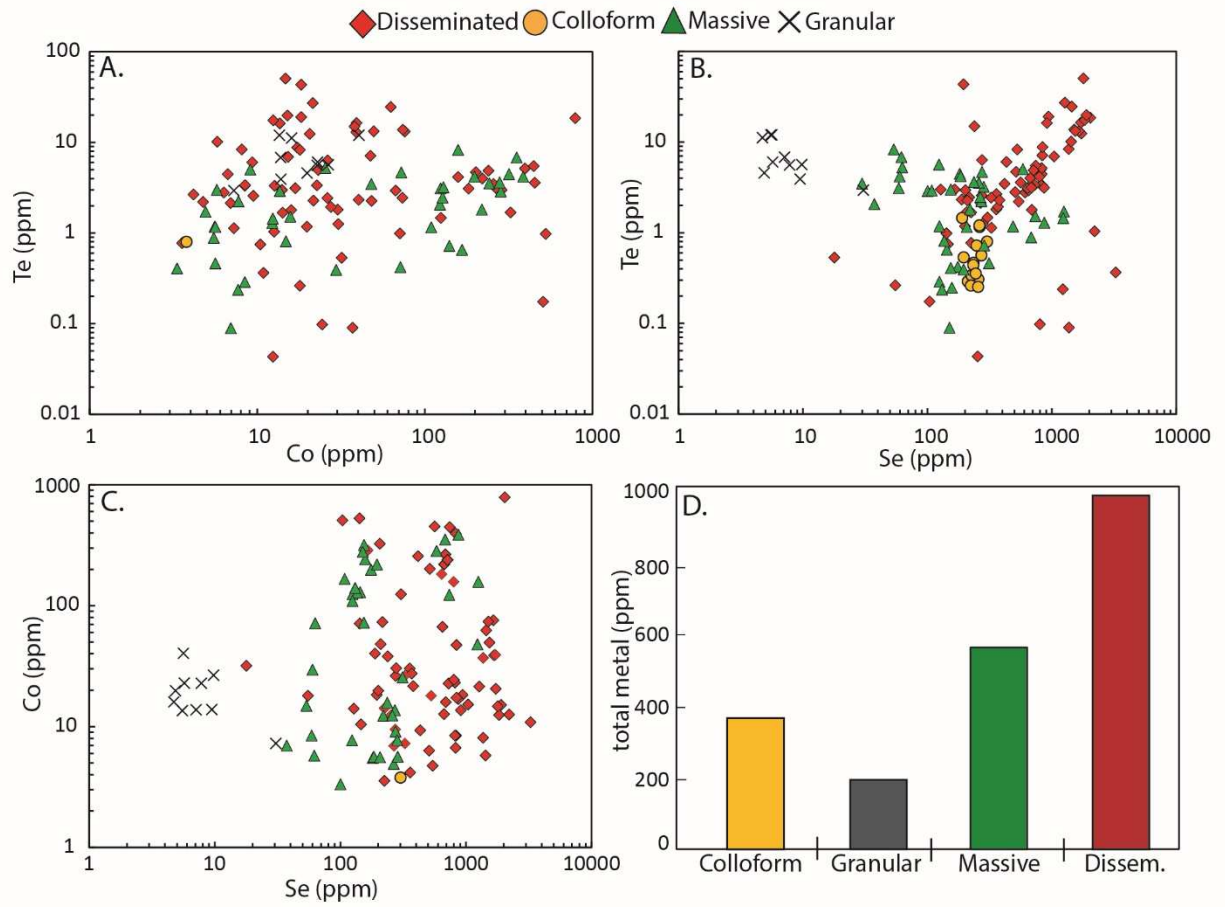


1051





1052



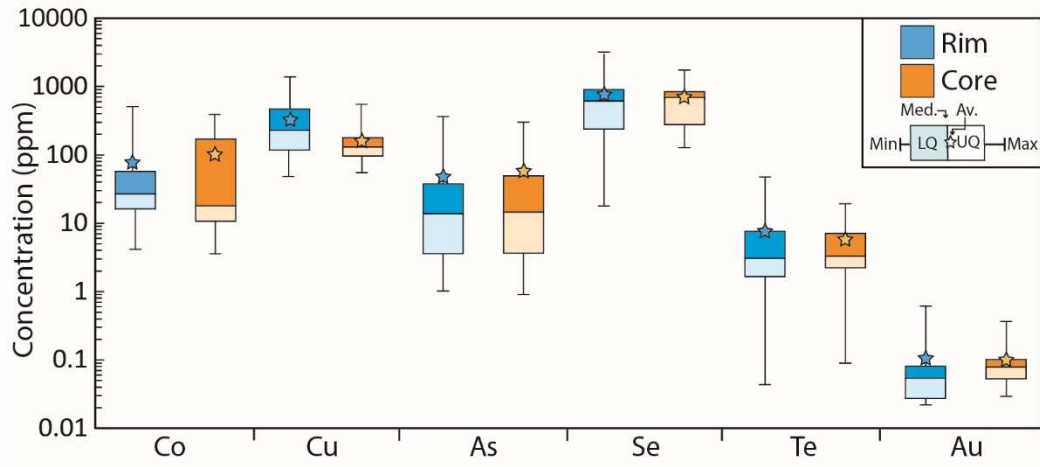
1053

1054

1055

1056

1057



1058

1059

1060

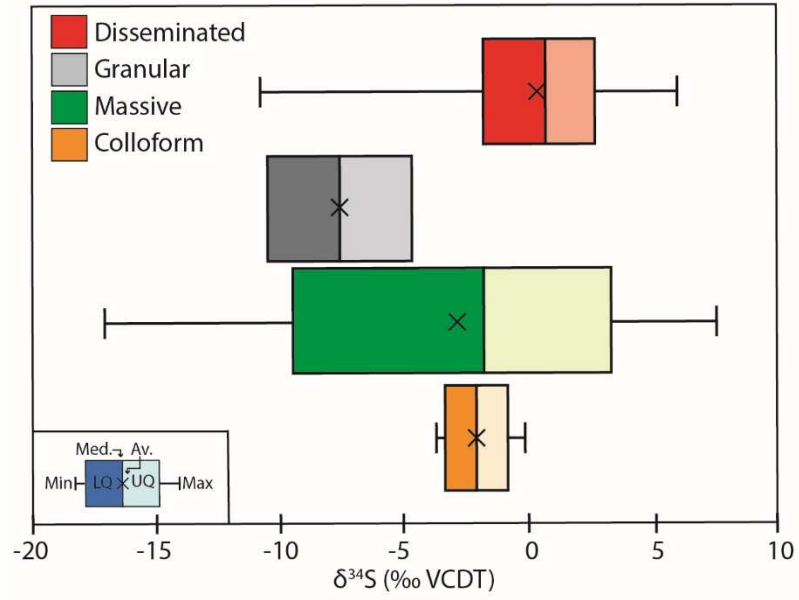
1061

1062

1063

1064

1065



1066

1067

1068

1069

1070

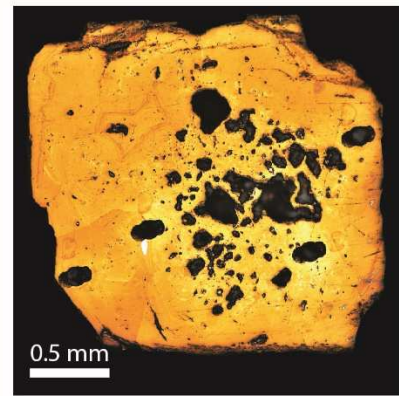
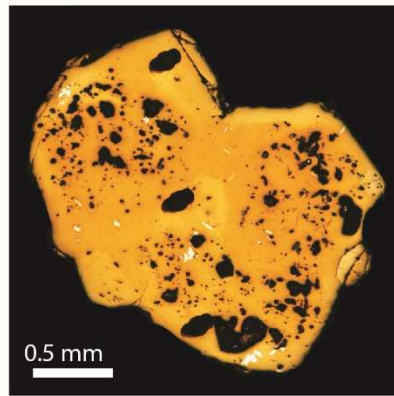
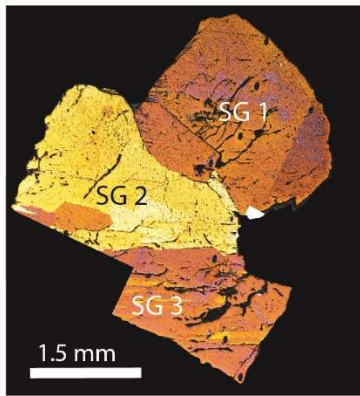
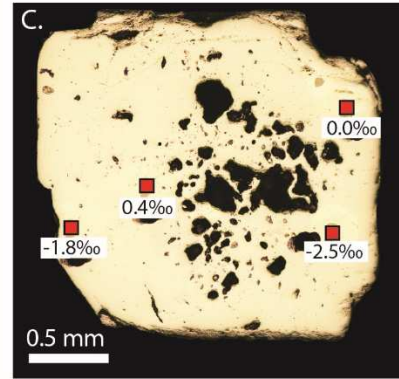
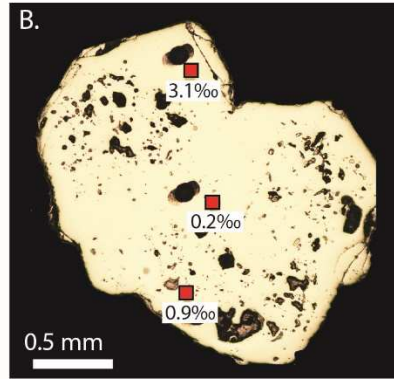
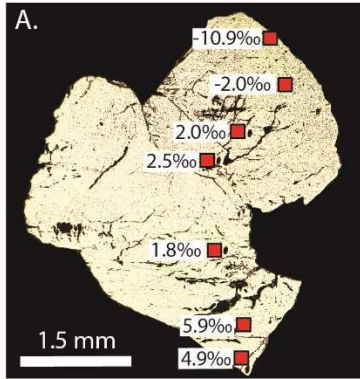
1071

1072

1073

1074

1075



1076

1077

1078

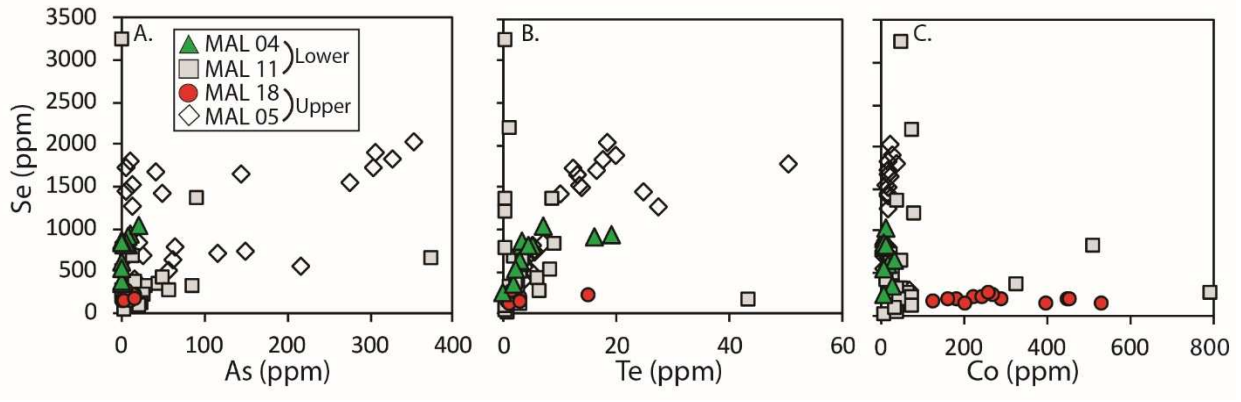
1079

1080

1081

1082





1083

1084

1085

1086

1087

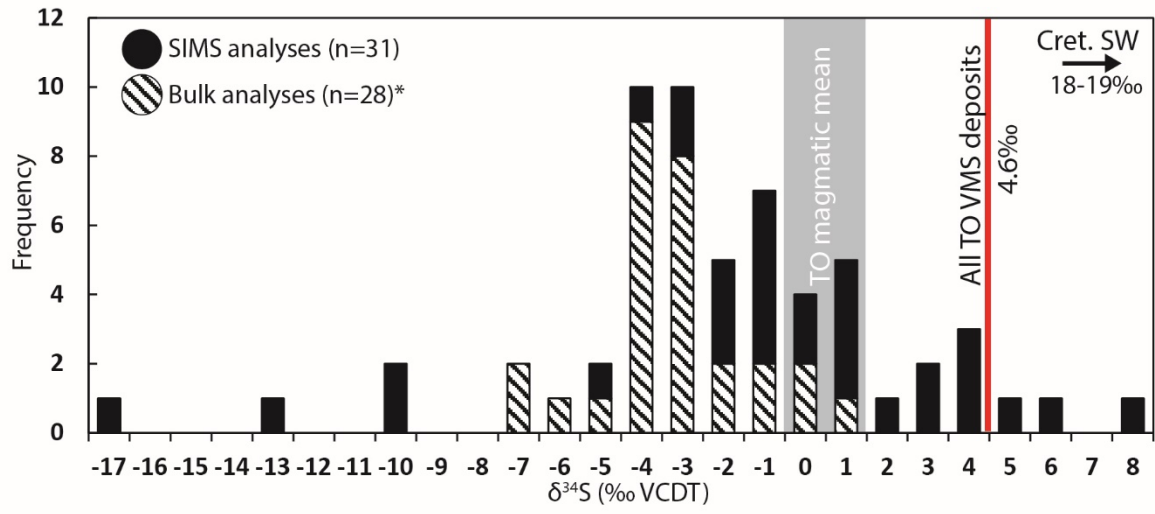
1088

1089

1090

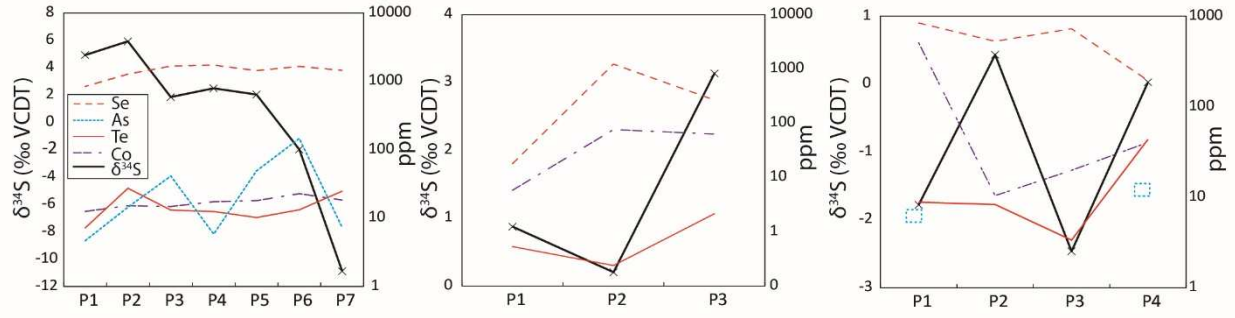
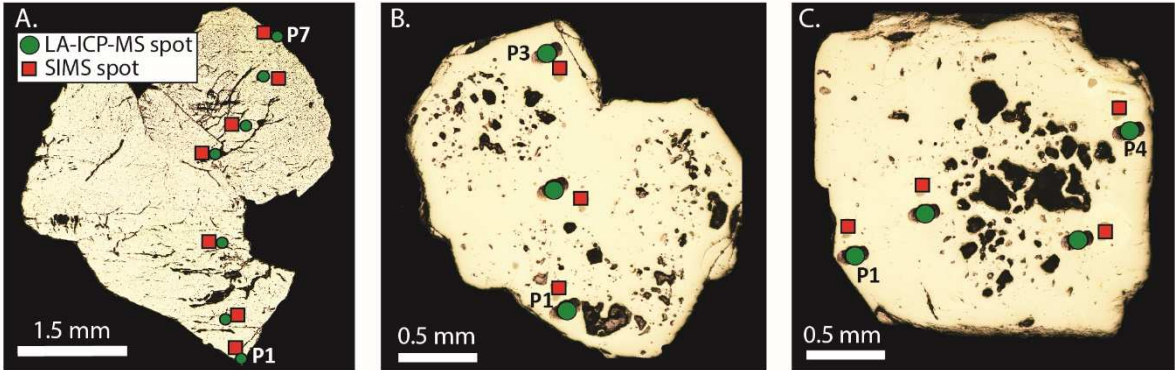
1091

1092

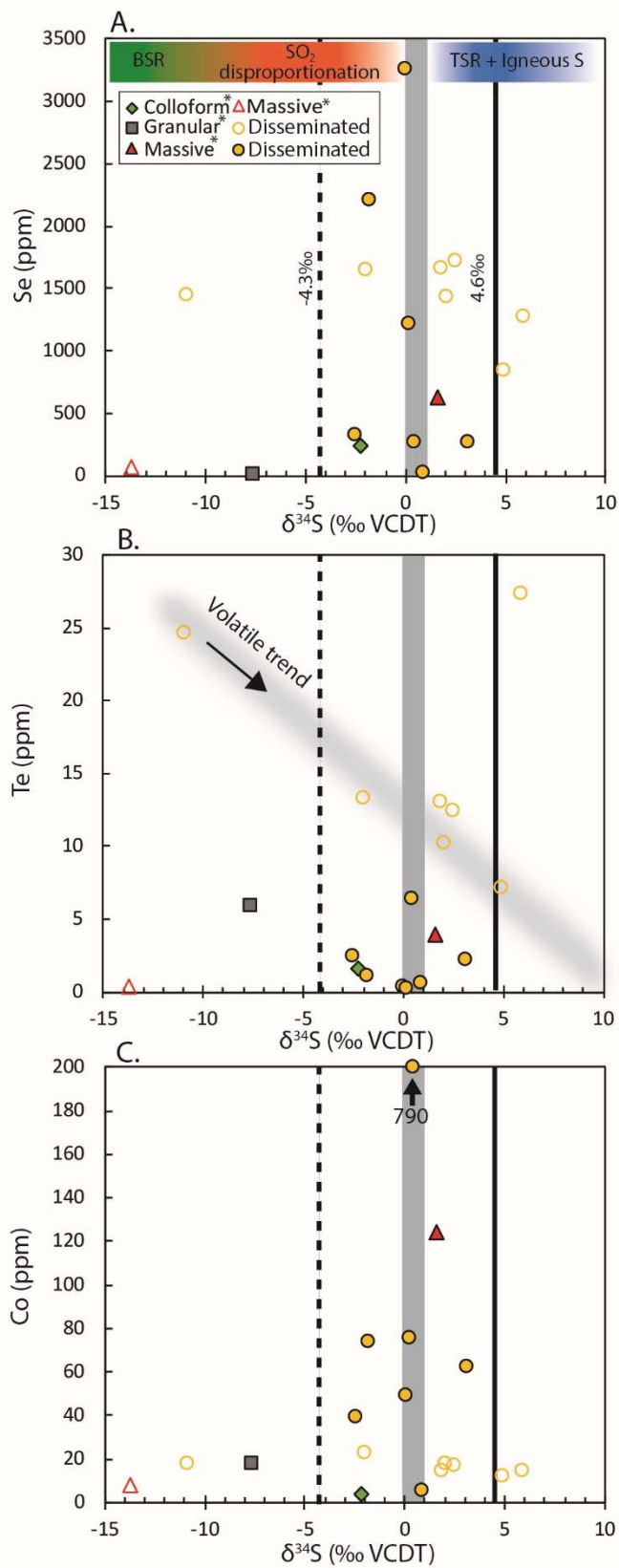


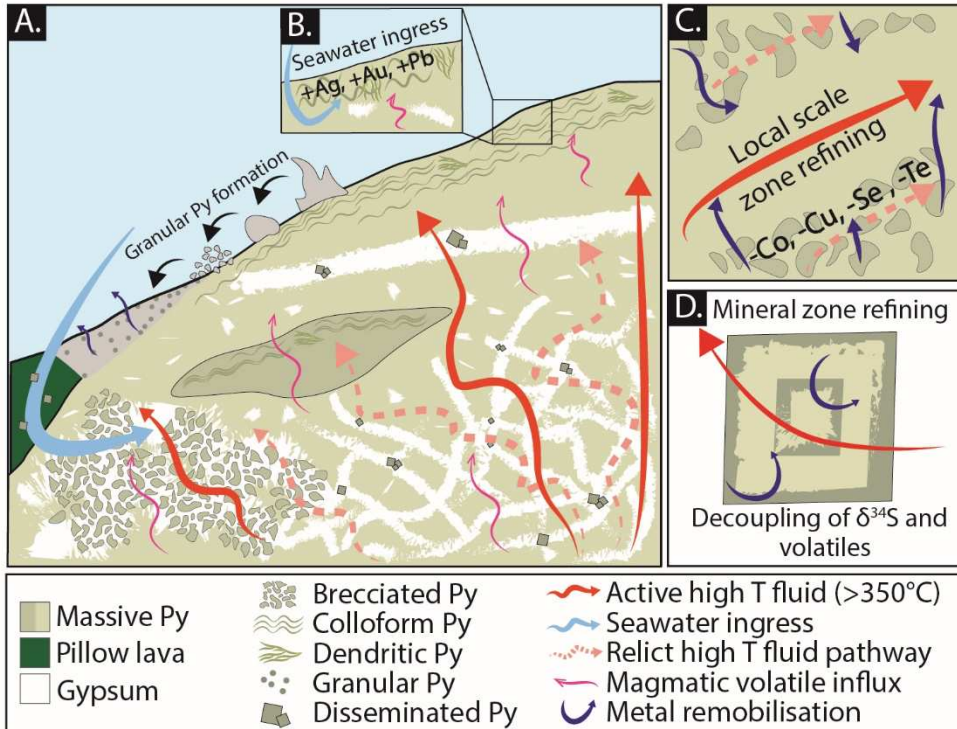
1093





1094





1096

		Colloform				Granular				Massive				Disseminated			
		Median	Min	Max	n > DL	Median	Min	Max	n > DL	Median	Min	Max	n > DL	Median	Min	Max	n > DL
Co	ppm			3.78	1	17.9	7.25	40.5	10	38.8	3.33	386.5	38	23.1	3.56	789.6	75
Ni	wt. %				0				0			0.01	1	0.01	0.01	0.07	12
Cu	wt. %	0.01	0.01	0.13	4		0.01	0.02	2	0.02	0.01	0.11	13	0.02	0.01	0.15	31
Zn	ppm		6.73	9.01	2				0	11.2	9.44	38.8	5	14.04	10.0	17.7	8
As	ppm	4.18	1.55	24.0	15	2.84	1.37	4.72	7	3.14	1.18	94.7	26	13.6	0.90	373.6	68
Se	ppm	244.6	195.9	301.7	15	6.40	4.72	30.6	10	178.3	29.8	1252.7	40	644.9	17.9	3260.7	78
Ag	ppm	0.24	0.15	0.49	15				0	0.42	0.16	0.89	11	0.24	0.19	0.33	7
Cd	ppm				0				0			0.26	1			0.67	1
Sb	ppm	0.47	0.25	1.46	15			0.35	1	0.97	0.16	5.76	14	0.25	0.22	1.14	3
Te	ppm	1.51	0.86	3.13	15	5.86	2.94	12.0	10	1.76	0.09	8.30	40	3.14	0.04	50.6	78
Re	ppm	0.17	0.11	0.25	15				0	0.15	0.03	0.83	17	0.05	0.01	1.80	35
Au	ppm	0.13	0.08	0.25	15		0.03	0.03	2	0.06	0.02	0.24	24	0.06	0.01	0.60	24
Pb	ppm	9.83	6.94	15.1	15				0	7.01	3.25	46.5	13	5.27	0.49	25.6	8
Bi	ppm	0.05	0.03	0.12	15			0.03	1	0.08	0.03	0.26	22	0.12	0.03	0.47	19

1097